High-resolution x-ray-scattering study of the commensurate-incommensurate transition of monolayer Kr on graphite

Peter W. Stephens
Department of Physics, State University of New York, Stony Brook, New York 11794

Paul A. Heiney* and Robert J. Birgeneau
Center for Material Science and Department of Physics, Massachusetts Institute of Technology, Cambridge, Massachusetts 02139

Paul M. Horn
IBM Thomas J. Watson Research Center, Yorktown Heights, New York 10598

David E. Moncton†
AT&T Bell Laboratories, Murray Hill, New Jersey 07974

George S. Brown
Stanford Synchrotron Radiation Laboratory, Stanford, California 94305
(Received 25 August 1983)

We report a detailed high-resolution, x-ray-scattering study of the commensurate-incommensurate transition of Kr on *ZYX* exfoliated graphite powder. As the Kr coverage is increased, the transition proceeds as follows: A sharp diffraction line from the commensurate phase drops in intensity and is replaced by a diffuse incommensurate line. The scattering from this disordered phase sharpens continuously as it moves to higher wave vector. We have followed this evolution up to 4% compression, where the line shape is adequately described by a power-law correlation function characteristic of two-dimensional solids. In one sample, there was a significant two-phase coexistence region which we ascribe to a distribution of critical points. We place an upper limit of 1% on the possible first-order jump. No evidence for a uniaxially compressed phase is seen. The weakly incommensurate diffraction line is accompanied by a satellite which may arise from either a domain-wall superlattice or a weak strain modulation of the overlayer. A detailed description of domain lattice models is presented. The loss of long-range order at the transition is discussed in the light of current theories.

I. INTRODUCTION

A high-density adsorbed surface layer represents a good example of a system with competing interactions; the periodicity preferred by the adsorbate-adsorbate interaction is typically not satisfied simultaneously with the modulation periodicity of the substrate. When the substrate periodicity is dominant, the adsorbed atoms occupy sites commensurate with the underlying surface. On the other hand, when the adsorbate-adsorbate interaction dominates the modulations in the adsorbate-substrate interaction, the surface layer will be incommensurate with the underlying substrate. When these interactions are comparable, an ordered commensurate (C) surface layer can undergo a transition into an incommensurate (IC) phase as a function of temperature or density. It is by now well known that competing interactions can lead to unusual phases of matter. Therefore, it is not surprising that the weakly incommensurate surface layer is a phase of considerable scientific interest. Indeed, one of the most intriguing features of the commensurate-incommensurate transition (C-ICT) stems from the suggestion by Frank and van der Merwe over 30 years ago, that the weakly IC surface layer should be composed of locally C regions separated by a periodic array of misfit dislocations (discommensurations).

Perhaps the best known example of the C-ICT occurs in the krypton monolayer adsorbed on the basal-plane surface of graphite. In this particular example the Kr-carbon interaction favors Kr adsorption sites which are centered over carbon hexagons of the graphite (001) basal plane. At low coverages the C-phase krypton layer solidifies into a $(\sqrt{3}\times\sqrt{3})R\,30°$ triangular solid. As the coverage is increased, this relatively loosely packed structure gives away to an IC triangular lattice with a lattice constant quite close to that of bulk krypton.

Until recently, attention on this system was focused on the related questions of whether the transition was continuous or first order, whether a description of the weakly IC phase in terms of a lattice of dislocations was appropriate, and whether the compression was uniaxial or preserved the hexagonal symmetry of the C phase. In a previous paper, we reported the discovery of a disordered phase separating the C and IC phases. In this paper we present the results of a detailed synchrotron x-ray-scattering study of this transition and the disordered weakly IC phase. As will become clear below, many of our results were only obtainable using a synchrotron

source for high x-ray intensity. In this paper we report details of new experimental runs as well as the previous studies.

The remainder of this paper is organized as follows. In Sec. II we review the state of understanding of the *C-IC*T of Kr on graphite prior to this work. In Sec. III we give the details of sample preparation and characterization, x-ray measurement technique, and line-shape analysis. In Sec. IV we discuss the data on the *C* side of the transition and in Sec. V we discuss the *IC* phase. In Sec. VI we describe the region in the immediate neighborhood of the transition. Finally, in Sec. VII we summarize our current understanding of this problem.

II. REVIEW

The essential element of all modern theories of *C-IC*T is the original Frank—van der Merwe suggestion that adsorbate-substrate mismatch is accommodated by localized discommensurations (or misfit dislocations) in the adsorbate lattice.[1] The original calculation was a continuum mean field or Landau model for a one-dimensional (1D) adsorbate lattice. Within this model the discommensuration density (or misfit) varies as the logarithm of the controlling parameter (the difference between the substrate and adsorbate natural lattice constants). However, the two-dimensional (2D) nature of the present physical system introduces new considerations. The point discommensurations of the 1D model become line defects or domain walls in two dimensions. Furthermore, these walls can meander and/or intersect. One can then imagine an *IC* phase compressed in only one direction represented by a striped array of parallel domain walls, or a uniformly compressed adsorbate corresponding to a network of locally *C*-phase hexagons. If the average distance l between domain walls is sufficiently large, then the wall-wall repulsion decays exponentially with distance, and the zero-temperature structure is controlled by only two factors: the domain-wall energy per unit length W and the wall-crossing energy Λ. Using Landau theory, Bak *et al.* predicted one of two possibilities depending on the sign of Λ.[2] If Λ is negative, there should be a first-order transition from the *C* phase to a hexagonal incommensurate (*HIC*) phase. Λ positive should lead to parallel domain walls in a striped incommensurate (*SIC*) phase. This latter transition was found to be continuous and, as in the Frank—van der Merwe theory, the misfit is proportional to the logarithm of the driving field. At higher incommensurability, the *SIC* phase could transform to a *HIC* phase through a first-order transition.

All of the models described above suffer from the same defect: Landau theories ignore thermodynamic fluctuations. Given the ground-state degeneracy of the experimental system, it is not clear that these theories will be valid even at $T=0$. Furthermore, as we shall discuss below, fluctuation effects can be so profound as to completely alter the nature of the *C-IC*T.

The first attempt to incorporate fluctuation effects was a calculation by Pokrovsky and Talapov who treated the *C* to *SIC* transition at finite temperature. They found that domain-wall meandering leads to an effective long-range repulsion between nominally parallel walls;[3] consequently, the density n above the commensurate density n_0 is proportional to the square root of the excess chemical potential, i.e.,

$$n-n_0=(\mu-\mu_c)^{\beta} \text{ with } \beta=\tfrac{1}{2} .$$

Recently, this prediction has been experimentally confirmed in a quasi-2D system undergoing a uniaxial *C-IC*T, stage-4 Br-intercalated graphite.[4]

The validity of the Pokrovsky-Talapov theory requires that the *IC* phase be stable with respect to formation of dislocations, i.e., a solid. However, as we shall discuss below, the experimental situation for Kr on graphite suggests otherwise. Specifically, fluctuation effects are so large as to destroy the long-range order of the weakly *IC* phase well below the accepted melting temperature. This experimental observation motivated theoretical work along two principal directions.

Villain had previously shown that for a given excess density, the honeycomb pattern of domain walls describing a *HIC* phase contains extra entropy in breathing modes.[5] Because any hexagonal domain can grow at the expense of its neighbors without changing the total wall length, a large number of topologically equivalent configurations will have the same energy. For sufficiently small positive Λ, this extra entropy stabilizes the *HIC* phase. However, the Villain fluctuations do not destroy the 2D power-law singularity in the structure factor, and therefore cannot explain the observed loss of quasi-long-range order. Subsequently, Coppersmith *et al.* have pointed out that under appropriate conditions this extra entropy softens the weakly *IC* phase to the extent that it becomes unstable to free dislocation formation, i.e., it is a fluid.[6] Because the free energy of interaction between domain walls is entropic and hence linear in temperature, they predict that the disordered phase extends down to $T=0$. Abraham *et al.* performed molecular-dynamics simulations which show a disordered network of domain walls in the overfilled monolayer.[7] Villain and Bak have found similar behavior in an Ising model with competing interactions.[8] Both the Villain[5] treatment and its refinement by Coppersmith *et al.*[6] are mean-field models in the sense that the average domain separation l is obtained by minimizing the free energy with respect to variations of l. Consequently, they predict that the *C-IC*T is first order. Coppersmith *et al.* argue, however, that the first-order jump should be quite small, and that the transition should be essentially continuous.

Kardar and Berker have argued that the three degenerate sublattices present in the *C* phase give rise to two types of domain walls with different energies. The system can then be mapped onto a helical Potts model.[9] They find an order-disorder transition in the three-state Potts universality class, and the *C-IC*T therefore has a specific-heat exponent $\alpha=\frac{1}{3}$. This leads to an excess density $n-n_0 \propto (\mu-\mu_c)^{2/3}$.

Huse and Fisher have extended the helical Potts-type models to the limit where the energy difference between the two domain walls is large.[10] In this limit the *C-IC*T is an order-disorder transition in a new universality class.

Bak has advanced a different explanation of these results; in a mean-field treatment of a model Ising system which exhibits a *C-IC*T, he finds chaotic phase-space trajectories between *C* and periodic *IC* phases.[11] He argues that this would produce a barrier to equilibration and hence a diffuse line shape. Similar results have been obtained by Pokrovsky for the phase-space trajectories of the Frank–van der Merwe model in one dimension.[12] He finds a phase of pinned solitons between the *C* and *IC* phases. However, the applicability of these pinned domain-wall models to the relatively high temperatures at which the experiments have been performed remains to be demonstrated.

The two theoretical pictures differ principally on the issue of whether the disorder is static or representative of thermal fluctuations, a question which remains to be addressed experimentally. It should be emphasized that neither of these approaches has been developed to the extent of predicting scattering profiles. The current state of the theory of *C-IC*T's has been reviewed by Bak, with an emphasis on the role of chaos.[13]

In contrast to the theoretical situation, the experimental results for krypton on graphite appear to be rather more straightforward. The existence of the *C-IC*T was first deduced from vapor-pressure isotherm measurements by Thomy *et al.*[14] The actual change of the Kr lattice constant was first measured by Chinn and Fain using low-energy electron diffraction (LEED) at temperature T, in the range 52–57 K.[15] They found that the misfit ϵ between the Kr lattice constant and its *C*-phase value went to zero continuously as the vapor pressure was reduced to a critical value. These results were interpreted in terms of the Frank–van der Merwe 1D model of local epitaxy. The high-pressure phase was found to be a hexagonal *IC* solid.

X-ray measurements at $T=80$–90 K, having somewhat higher resolution than the LEED experiments, confirmed the LEED description as a transition from *C* to *HIC* phases, and set a somewhat tighter upper limit of 1% on the first-order jump in lattice constant.[16] Satellite lines were observed as the principal Kr diffraction peak moved from its *C*-phase position, and these were interpreted as evidence for hexagonal domain walls[16] or a triple-$\vec{q}$ sinusoidal strain wave in the Kr monolayer.[17] In addition, the difference ϵ between the peak position and its *C*-phase value was found to depend on the chemical potential μ as

$$\epsilon = A\,[\mu-\mu_c(T)]^{\beta}\,, \tag{1}$$

with $\beta=0.33\pm0.03$. Figure 1 shows ϵ vs $\mu-\mu_c$ for all of the constant-temperature diffraction data, together with a fit to Eq. (1). As first noted by Fain *et al.*, A and β are independent of T, a strikingly simple result.[18]

There has been a certain amount of controversy surrounding the question of whether the observed power-law dependence of ϵ on μ can be considered a critical behavior. Schabes-Retchkiman and Venables regard the power-law form of Eq. (1) as a coincidence relating to the details of interatomic force law.[19] They calculate the lattice constant for a free 2D film, to which they then apply the Frank–van der Merwe result relating the domain-wall density to the difference in natural lattice constants and obtain apparent agreement with experiment. Shiba has derived similar results,[20] as well as accounting in detail for the observed adsorbate rotation at about 2% misfit.[18] However, in light of the importance of domain-wall meandering,[3] these calculations cannot be regarded as conclusive. It has also been argued that Eq. (1) with $\beta\sim\frac{1}{3}$ is an accidental crossover effect between various limiting cases.[21] Kardar and Berker[9] speculate that the incoherent structure of the domain-wall lattice yields $\epsilon\propto(n-n_0)^{1/2}$, leading to $\beta=\frac{1}{3}$. Huse and Fisher do not address the excess density; indeed they discuss the diffraction peak shift directly. They find $\beta=\nu\geq\frac{1}{2}$, and suggest that the experimental results are dominated by crossover effects.[10] However, ϵ is observed to be a function only of the chemical-potential difference $\mu-\mu_c$ over a wide range in temperature (52–94 K). Crossover between zero- and finite-temperature descriptions or between critical behavior and saturation would be expected to depend on temperature. Clearly, a more quantitative analysis is required. We can only conclude that the experimentally simple variation of ϵ with chemical potential has not been unambiguously explained.

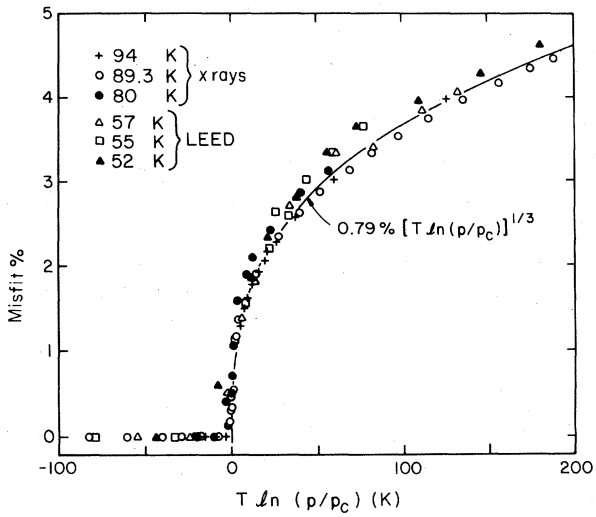

FIG. 1. Peak shift ϵ vs chemical potential difference at a series of temperatures for Kr on graphite. The squares and triangles are LEED data from Refs. 15 and 18, the circles are x-ray data from Ref. 16, and the crosses are from the present work.

In a related experiment, Nielsen *et al.* observed a first-order jump of 1.8% in lattice constant when the Kr monolayer was compressed by coadsorption of deuterium at the relatively low temperature of 40 K.[22] If this first-order jump is characteristic of a pure Kr adsorbate, then there must be a dramatic evolution of the phase boundaries, perhaps a tricritical point, in this neighborhood. On the other hand, a difference in D_2 solubility between *C* and *IC* phases of Kr could cause a first-order transition in the mixed system.[9]

A qualitatively new picture emerged with the application of synchrotron x-ray techniques having an intrinsic

wave-vector resolution sharper than the finite size of the sample crystallites.[23] We found that the sharp C-phase diffraction peak gave way to a broad IC-phase peak, and that as the coverage was increased, the IC peak became sharper as it moved to larger wave vector. Thus the weakly IC phase is disordered. The width of the diffraction peak in the weakly IC phase is on the order of its incommensurability ϵ. Despite the changes in diffraction-profile shape, the incommensurability still follows Eq. (1).

In order to characterize this interesting system better, we have extended our higher-resolution measurements of the structure of Kr on graphite in the neighborhood of the C-ICT. In addition to a full account of the previous high-resolution experiment, this paper reports data taken at Stanford Synchrotron Radiation Laboratory (SSRL) on an eight-pole wiggler magnet, and with a torroidal focusing mirror of improved reflectivity; these technical improvements led to a 240-fold increase in counting rate so that data with much better statistics than before were obtained. This in turn yielded a more accurate view of certain aspects of the transition. In all, data from three sets of scans through the transition are reported here: the earlier closed-cell-I data taken with bending-magnet radiation, and a closed-cell-II and a constant-temperature scan using the wiggler beam line. The approximate paths through the phase diagrams are shown in Fig. 2. The basic conclusions from the previous work remain unchanged, although the improved statistics show that none of the line-shape models we have considered is able to reproduce the experimental data very near the transition.

Figure 3 shows sequences of diffraction profiles taken in two passes through the transition: changing temperature (and therefore coverage) with a fixed amount of Kr in the sample cell, and changing vapor pressure at constant temperature. (Figure 2 of Ref. 23 shows the same evolution in the closed-cell-I data.) In both sets of data we see the following evolution as the system passes from C to IC phases: The first two scans show a sharp C-phase peak at 1.700 Å^{-1} which decreases markedly in intensity upon approaching the transition. The evident asymmetry in the peak shape is simply a geometric effect related to the graphite powder distribution; it is discussed in the next section. The third and fourth scans each show a composite line shape in which the sharp C-phase peak trades intensity with a much more diffuse line. Finally, the last two scans show the evolution toward increasing incommensurability with a satellite line apparent below the C-phase vector. Clearly, the evolution through the C-IC T is rather complex. We shall present the data in detail as well as an analysis for each of these regions in turn in subsequent sections of this paper.

III. EXPERIMENTAL DETAILS

The substrate was ZYX exfoliated graphite,[25] manufactured by intercalating highly ordered pryolitic graphite and carefully exfoliating it. ZYX has a surface area of 1–3 m^3/g (equivalently, 1–3 m^2/cm^3). Detailed x-ray analysis motivated by our original synchrotron work[23,26] shows it to be comprised of crystallites with lateral extent of at least 3000 Å and thickness on the order of 1000 Å.[27] The c axes (perpendicular to the basal planes) are more or less parallel, with a distribution of some 10° halfwidth at half maximum (HWHM). The density is about one-half

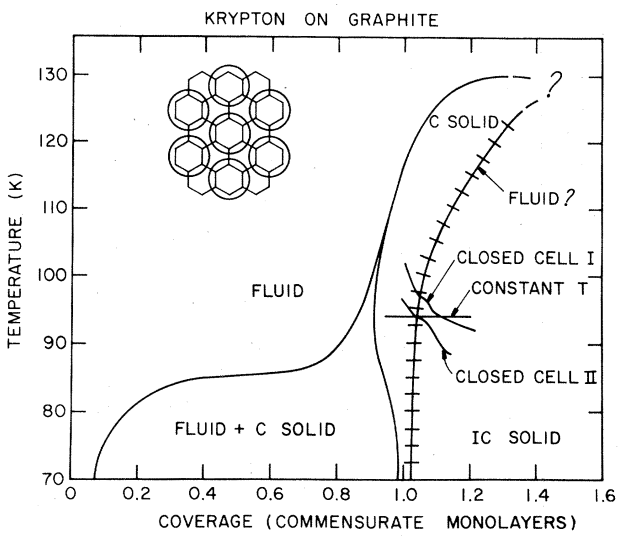

FIG. 2. Phase diagram of Kr on graphite. Inset shows the $(\sqrt{3}\times\sqrt{3})R30°$ structure of C-phase solid. The phase boundary lines come primarily from the specific-heat studies of Butler *et al.* (Ref. 24). The paths for the three data sets in the present work are also shown.

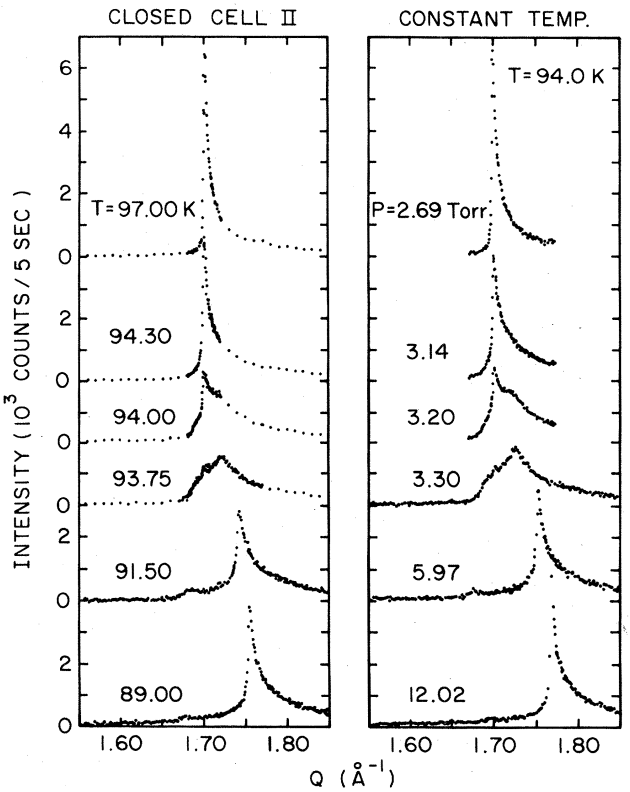

FIG. 3. Scans showing the evolution from C- to IC-phase line shape in the closed-cell-II and constant-temperature data sets. In all data shown in this paper, 95% of the empty-cell background has been subtracted from the data.

that of solid graphite. For vapor pressures of a few Torr, we typically find an equilibration time of 5 min; evidently the empty spaces are well connected. The samples were cut to $1.2\times1.2\times0.2$ cm^3 (c axis in the thin direction) and baked at 800 °C in a 10^{-5}-Torr vacuum for 1 h. The sample for the original run reported in Ref. 23 was promptly loaded into a sample cell in a dry N_2 glovebox; the sample on which the more recent data were taken was wrapped in Grafoil and sealed in a vial for the 1 yr that elapsed between experiments.

The sample holders used for both experiments were made of Al, with cylindrical Be windows attached with epoxy and a total volume of 4.3 cm^3. They were mounted in an Air Products Displex cryostat with a Si-diode temperature sensor capable of controlling temperature to 0.05 K. The sample was dosed with a trapped, diffusion-pumped vacuum system with a base pressure of about 10^{-6} Torr. MKS Instruments Baratron capacitance membrane manometers were used to measure the dosing pressure. The closed-cell-I run was performed with the same Kr dose as an experiment on the melting of commensurate Kr.[26] The runs on the wiggler magnet were taken immediately before an experiment on the melting of Xe, using the same sample of graphite.[28] In the Xe experiment at 1.1 monolayers, we observed a continuous evolution of the liquid correlation length up to at least 200 Å. As discussed below, rounding of the *C-ICT* set in at roughly the same length scale.

The first run was carried out on a bending-magnet beam line at SSRL, whereas the second run used wiggler beam line VII.[29] Typical storage-ring parameters were 3.0 GeV and 60 mA. In both cases, the x-ray beam was focused by reflection at a grazing angle from a bent toroidal mirror onto the sample position. Two parallel Ge(111) or Si(111) crystals selected an incident wavelength of about 1.70 Å, and the scattered radiation was analyzed by reflection from a Ge(111) crystal. The crystals and sample alternately deflected the beam up and parallel to its initial direction, so that the overall configuration was approximately nondispersive. In the region of 1.7 Å^{-1}, the longitudinal resolution is ~0.0003 Å^{-1} HWHM. For the wiggler run, the x-ray flux on the sample was 10^{12}–10^{13} photons/sec in a spot 2×4 mm^2. The scattered x rays were detected by a scintillation detector. An incident-beam monitor controlled the counting time for each data point. Unfortunately, the beam-monitor sensitivity changed several times during the experiment due to electron-orbit shifts and thermal expansion of the mirror. We have, therefore, normalized intensities relative to scans of the graphite (002) diffraction peak which were measured frequently during the course of the run.

The Kr in the cell absorbed a fraction of the incident beam. This lowers the background from its empty-cell value (~100 counts/sec), which in turn can have an important effect on the weak wings of diffraction line shapes. We estimated this absorption to be 5% from the density of Kr in the cell, and verified that the peak of the graphite (002) reflection decreased by roughly that amount. Scans reported have 95% of the empty-shell background subtracted.

The powder nature of the graphite substrate plays an important role in determining the line shape. First, the 2D scatterer produces Bragg rods in reciprocal space perpendicular to the plane of the adsorbate. In effect, the condition for constructive interference of scattered waves places no constraint on the component of the wave vector perpendicular to the layer of atoms. Second, because the graphite crystallites are rotationally disordered about their c axes, the Bragg rods become cylinders. Finally, the distribution of c-axis inclinations about the perpendicular to the scattering plane produces scattering at wave vectors that are generally larger than the cylinder's radius, leading to the sawtooth line shape characteristic of 2D powders. This line shape was analyzed by Warren for the case of completely random c-axis orientation.[30] Kjems *et al.* used the Warren line shape as the basis for an approximation for partially ordered substrates such as Grafoil and *ZYX* that has subsequently been widely used in analysis of neutron and x-ray measurements.[31] In the Appendix, we discuss the applicability of this modified Warren form and derive the general expression for the powder-averaged line shape that has been used in previous work by this group.

IV. COMMENSURATE PHASE

The scattering from a C-phase monolayer has been previously investigated under sufficiently high resolution where the crystallite size dominates the peak width.[26] However, this is the first study with sufficiently good counting statistics for measuring the structure directly, rather than merely extracting a characteristic length.

In previous work,[16,23,26] the C-phase peak was fit to a Gaussian with HWHM equal to π/L, where L is taken as a characteristic dimension of the scattering array,

$$I(\vec{Q})=\frac{1}{\pi\gamma^2}\exp-(|\vec{Q}-\vec{Q}_{\rm comm}|/\gamma)^2 , \tag{2}$$

where $\gamma=\pi/(L\sqrt{\ln2})$, and $\vec{Q}$ and $\vec{Q}_{\rm comm}$ are in the crystallite plane. The top panel in Fig. 4 shows a least-squares fit of a scan in the C phase to an appropriately powder-averaged Gaussian. Clearly, the model, which has a width fixed primarily by the fastest-rising data points, cuts off in the wing much faster than the experimental data. In order to account for this extra scattering, we develop a more precise model for the finite-size cutoff of a Bragg peak in two dimensions.

By considering a static hexagonal domain of a triangular lattice, pictured in Fig. 5(a), the structure factor is

$$S(\vec{Q})=1+\sum_{j=1}^{N-1}\sum_{k=0}^{N-1}\{\exp[i\vec{Q}\cdot(j\vec{r}_1+k\vec{r}_2)] +\exp[i\vec{Q}\cdot(j\vec{r}_2+k\vec{r}_3)] +\exp[i\vec{Q}\cdot(j\vec{r}_3+k\vec{r}_1)]\} , \tag{3}$$

where $\vec{r}_1$ and $\vec{r}_2$ are lattice vectors of length a, 120° apart, and $\vec{r}_3=-\vec{r}_1-\vec{r}_2$. Summation of the geometric series yields

$$S(\vec{Q})=\{\sin(N\vec{Q}\cdot\vec{r}_1)+\sin(N\vec{Q}\cdot\vec{r}_2)\sin(N\vec{Q}\cdot\vec{r}_3)-\sin[(N-1)\vec{Q}\cdot\vec{r}_1]$$
$$-\sin[(N-1)\vec{Q}\cdot\vec{r}_2)-\sin[(N-1)\vec{Q}\cdot\vec{r}_3]\}[\sin(\vec{Q}\cdot\vec{r}_1)+\sin(\vec{Q}\cdot\vec{r}_2)+\sin(\vec{Q}\cdot\vec{r}_3)]^{-1}\ . \quad (4)$$

Equation (4) reaches its maximum value of $3N^2-3N+1$ (the total number of atoms) when $\vec{Q}$ is equal to an element of the reciprocal lattice. The function has a complicated pattern of side lobes around each Bragg peak. In a powder, a diffraction experiment measures the circular average $\int_0^{2\pi}|S(\vec{Q})|^2 d\phi$, where ϕ is the angle between $\vec{Q}$ and $\vec{r}_1$. This integral, calculated numerically, is plotted in Fig. 5(b). In order to parametrize this result, we show as a dashed line the sum of a Gaussian and a Lorentzian with equal halfwidths γ,

$$I_c(Q)=A\exp\left[-(Q-q_0)^2\frac{\ln 2}{\gamma^2}\right]+\frac{B\gamma^2}{\gamma^2+(Q-q_0)^2}\ , \quad (5)$$

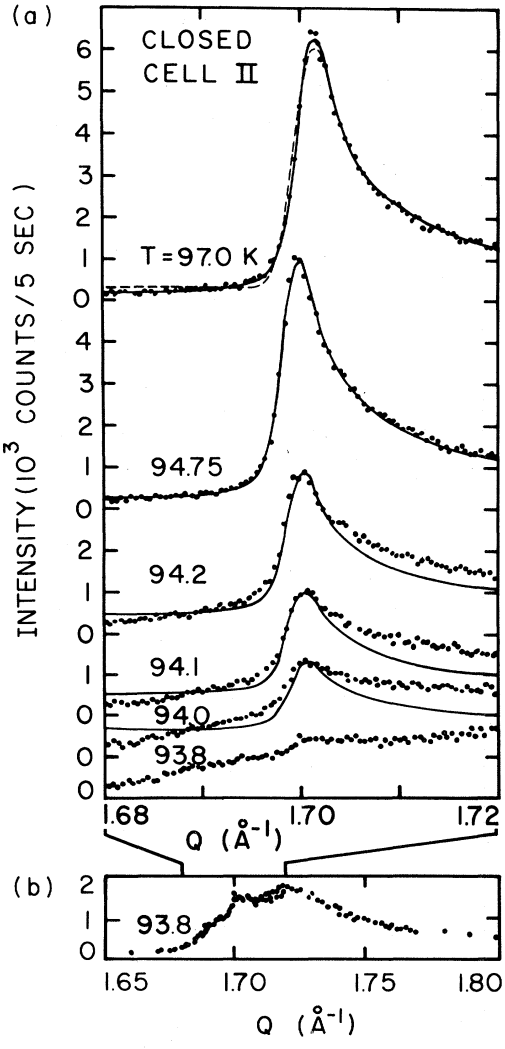

FIG. 4. Scans showing the destruction of long-range order of the C phase in the closed-cell-II run. The dashed line in the 97.0-K scan is a fit to a Gaussian line shape, suitably powder-averaged. Solid lines are fits to Gaussian plus Lorentzian with equal halfwidths, as discussed in the text. An adjustable constant background has been added to the model curve. Bottom panel shows the complete 93.8-K scan.

with the ratio of peak intensities B/A equal to 1.8. While Eq. (5) does not follow the ripples, it is clearly a very good approximation to the general shape of the circular average. A distribution of crystallite sizes would be expected to smooth out the ripples but retain a width on the order of the average crystallite size. The halfwidth γ is $1.7/Na\cong 2.96/L$, where $L=(N-1)a\sqrt{3}$ is the distance across the hypothesized hexagonal domain in the diffraction direction. We emphasize that it is the powder-averaged line shape rather than the intrinsic profile which has the q^{-2} tails;[32] an intrinsic q^{-2} term yields a much broader q^{-1} wing in a powder average.

We provide a crude estimate of the dynamics of a Kr monolayer as follows. If each atom of a harmonic solid with phonon spectrum $\omega_0(K)$ is attached to a fixed sub-

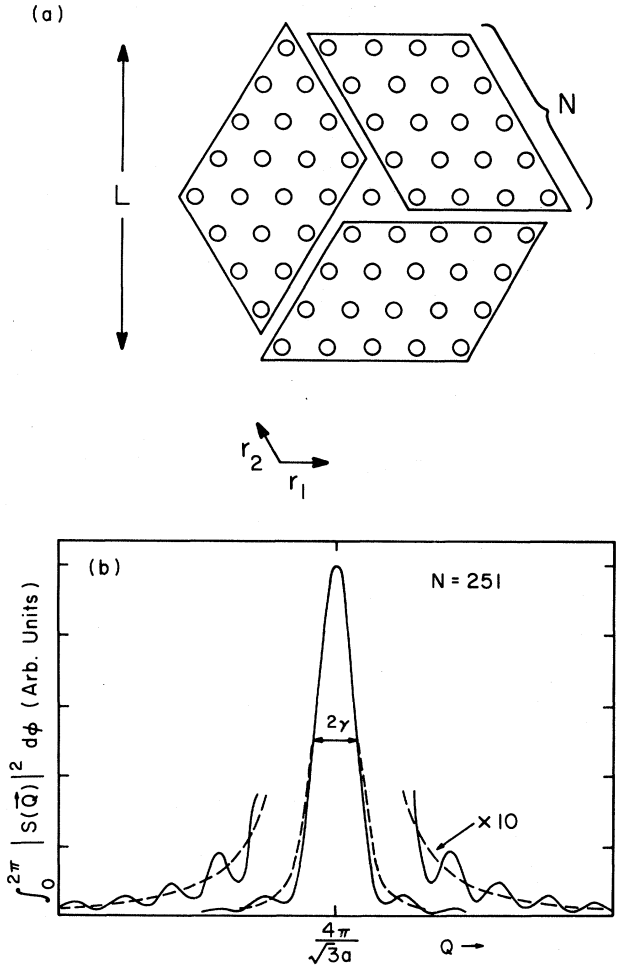

FIG. 5. Top shows the hexagonal domain of C-phase solid. Bottom shows the rotational integral of structure factor squared for the hexagonal domain near the (1 0) Bragg peak. Solid line denotes the numerical calculation. Dashed line denotes the approximation as sum of Gaussian plus Lorentzian with equal halfwidths.

strate by a spring constant ξ, the resulting dispersion relation is $\omega(K)=[\omega_0^2(K)+\xi/m]^{1/2}$. This creates a gap of energy $\hbar(\xi/m)^{1/2}=5K$ at zero wave vector.[33] The gap dominates the dynamics for wave vectors $K \lesssim (\xi/mc^2)^{1/2}$, where c is the (average) speed of sound in the freely floating solid. In three-dimensional (3D) Kr, $c=8\times10^4$ cm/sec, so that the C-phase phonon spectrum should be flat for wave vectors below ~0.05 Å^{-1}. Hence, the thermal diffuse scattering would be a Lorentzian with halfwidth ~0.05 Å^{-1} centered about each Bragg peak. Note, however, that the gap is expected to decrease to zero as the C-IC T is approached.[3,34]

Returning to Fig. 4, we see that the finite-size—cutoff model of Eq. (5) describes the line shape quite well sufficiently far from the transition. Likewise, Fig. 6 shows similar data for the closed-cell-I scans. The solid lines in Figs. 4 and 6 were fitted to the experimental data over the range 1.68—1.72 Å^{-1}. The model curves are given by Eq. (5), corrected for a vertical mosaic of 11° HWHM, plus an adjustable constant term which is discussed below. All of the model line shapes in Figs. 4 and 6 have HWHM fixed at 0.0016 Å^{-1}, leading to an estimate of the C-phase crystallite size of 1900±500 Å. This number is smaller than the 3000-Å lower limit on graphite crystallite lateral extent, perhaps due to steps or adsorbed impurities. In fact, because a single-atomic step destroys the coherence of a C-phase sublattice, 1900 Å may be taken as the lower limit of separation between single atomic steps.

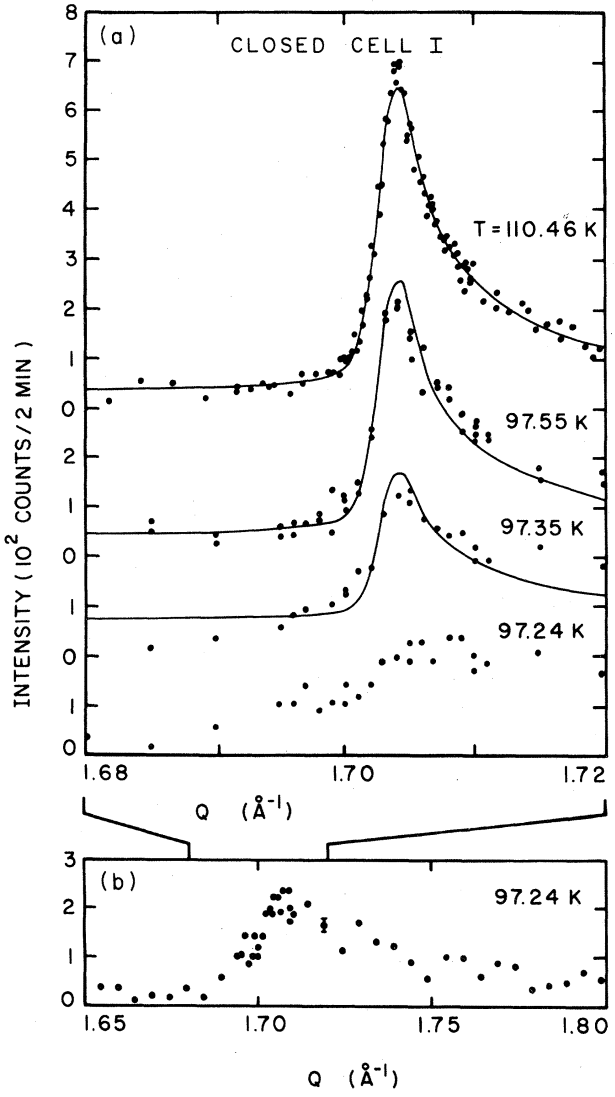

FIG. 6. Scans in C phase of closed-cell-I run, fitted to Gaussian-plus-Lorentzian model plus constant background.

We emphasize that it is the high resolution and good statistics which enable us to see that a simple Gaussian is not an adequate description of the commensurate line shape. On the other hand, it should be noted that the monochromator and analyzer which determine the spectrometer resolution have rocking curves with q^{-4} and q^{-2} tails, respectively. In general, these tails will produce q^{-2} wings on diffraction peaks. In the present case, these tails will be quite weak since the resolution is sharper than the intrinsic scattering cross section. Nevertheless, in the absence of more detailed knowledge of the spectrometer-resolution function, it is inappropriate to attach too much significance to the detailed shape of the wings observed in the C phase.

The scans in Figs. 4 and 6 clearly show that the baseline away from the peak is higher than the absorption-corrected empty-cell background. In both runs, as the coverage is increased (temperature reduced), this diffuse intensity increases and the Bragg-peak intensity decreases. Inspection of the broader scans in Figs. 3 and 4(b) shows that as the C-phase intensity drops, a much broader peak centered at 1.72—1.72 Å^{-1} is forming in the closed-cell-II scans. On the other hand, it is shown in Fig. 6(b) that the closed-cell-I C-phase peak gives way to a peak that is centered at (1.705±0.005) Å^{-1}. This profile is somewhat sharper than the end result of the closed-cell-II scans, and shows no trace of a coexisting C-phase peak. As is suggested in Fig. 3, the constant-temperature scans, taken with the same sample and under the same conditions as the closed-cell-II data, show an identical evolution. Clearly, we are observing a melting transition in which the C phase is replaced by a disordered phase.

In order to discuss this trade-off quantitatively, we plot the intensity of the peak (~1.70 Å^{-1}) and the baseline derived from the constant term in the line-shape model in Fig. 7. Let us first consider the closed-cell-I data. At the higher temperatures, the Bragg peak is superimposed on a diffuse background of ~40 counts/2 min. This background could be due to thermal diffuse scattering as discussed above; however, uncertainty in the background subtraction prevents us from determining the shape of this extra diffuse component. It is evident that the peak intensity drops and the diffuse scattering rises precipitously within a narrow temperature range around 97.5 K.

The closed-cell-II and constant-temperature scans show a similar evolution in Figs. 7(b) and 7(c). However, the region of composite C and IC profiles is manifested in a long tail of C-phase intensity down to 93.6 K. This is highly reminiscent of the rounding behavior in x-ray-scattering studies of the melting transition of C-phase Kr.[26,35] Because of this rounding in the closed-cell-II and constant-temperature data sets, we can only place a rough

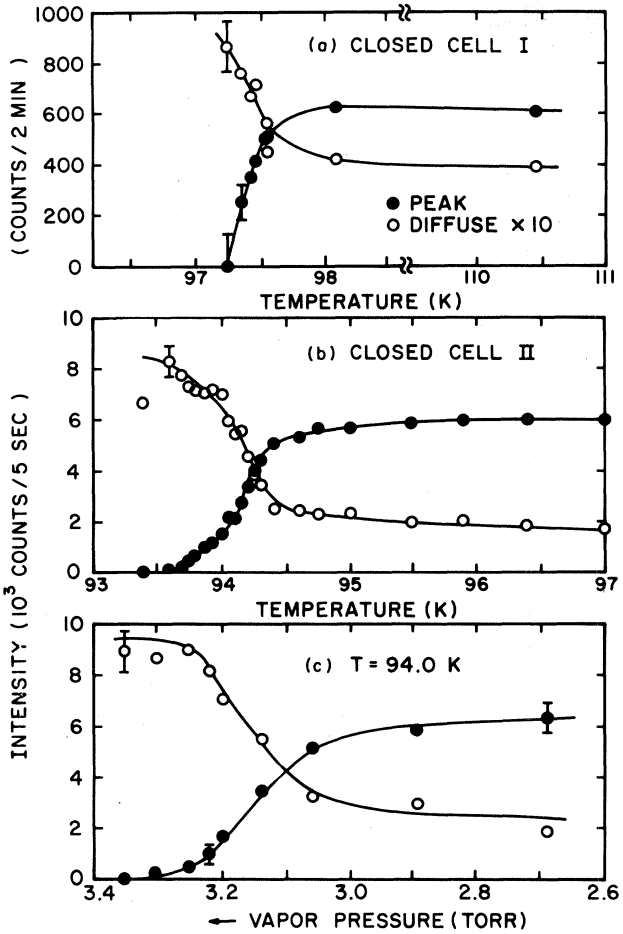

FIG. 7. Peak and background intensities for the C phase from the three experimental runs. Intensities were determined from fits such as those shown in Figs. 4 and 6. Smooth curves are guides for the eye.

upper limit on the degree of first-order character of this C-phase melting transition. Indeed, the square of the order parameter has dropped to only half of its saturated value when the composite nature of the line shape becomes clear. The issue is further complicated by the presence of critical scattering. We discuss this regime of composite line shape in Sec. VI; for now we simply point out that it could arise either from coexistence in a first-order transition or from an inhomogeneous broadening of the critical point.[36]

We emphasize that the possible rounding of the transition observed in two of the data sets does not alter the following principal conclusions of this section. (1) Away from the C-ICT, the C-phase line shape is well described by a model of finite-size domains. (2) The first stage in the transition to an IC phase is the loss of long-range order as evidenced by the disappearance of a sharp Bragg peak. The C phase is replaced by a liquidlike IC phase, with a correlation length much smaller than the crystallite size.

V. INCOMMENSURATE PHASE

We now turn to a description of the IC phase. In this discussion, the principal issue is the evolution of the diffraction line shape with changing incommensurability, particularly the loss of long-range order and the strain modulation caused by the competition between the graphite and Kr periodicities.

Figure 8 shows two IC scans from the constant-temperature data set. We first note that both scans have prominent wings which are absent from the C-phase scans. Consequently, we can immediately exclude a Gaussian line shape, even with a width much greater than that observed in the C phase.

To proceed further we briefly review the theoretical understanding of the structure of 2D solids. We express the deviation of each atom from its average lattice position $\vec{R}$ as a function $\vec{U}(\vec{R})$. By expanding $\vec{U}(\vec{R})$ in phonon modes, it can be readily shown that in two dimensions the position-position correlations decay as a power law,

$$\langle \vec{U}_\tau(\vec{R}),\vec{U}(\vec{0})\rangle \propto R^{-\eta_\tau},$$

where η_τ depends on elastic constants, temperature, and the wave vector at which the correlations are studied.[37] This algebraic decay of correlations leads to a scattering cross section

$$\frac{d\sigma(\vec{Q})}{d\Omega} \propto |\vec{Q}-\vec{\tau}|^{-2+\eta_\tau},$$

for $\vec{Q}$ in the neighborhood of a Bragg peak $\vec{\tau}$. Of course, in a real experiment the measured extent of correlations is limited either by the finite size L of the sample crystallites or by finite resolution. Nevertheless, the algebraic decay of correlations is observable in scattering experiments, as

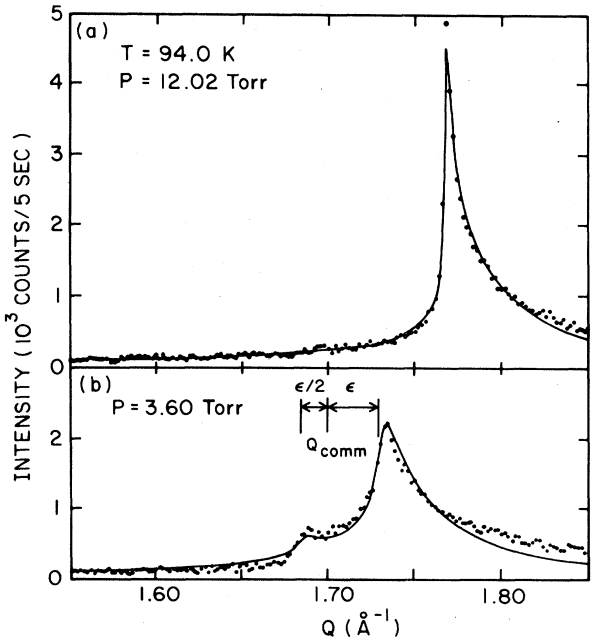

FIG. 8. Two scans in the IC phase from the constant-temperature data set. The solid line in the top panel is a fit to a finite-size—cutoff powder-averaged power-law line shape $Q^{\eta-2}$ with $\eta=0.3$. The bottom panel shows fit to two powder-averaged Lorentzian line shapes centered about $Q_{\rm comm}+\epsilon$ and $Q_{\rm comm}-\epsilon/2$.

shown by Moncton and Pindak[38] in the resolution-dominated case, and by Dutta and Sinha in the finite-size–dominated regime,[39] appropriate here.

Figure 8(a) is fitted to the finite-size–cutoff model of Dutta and Sinha, with η fixed at 0.3, the same value as measured for *IC*-phase solid Xe several K below its melting temperature.[28] In this scan the lattice constant is 4.0% smaller than the *C*-phase value (4.27 Å), a misfit two-thirds as great as that of the expanded Xe monolayer. Clearly, the power-law–singularity form works very well, thus suggesting that at this density the Kr forms a floating solid. The lower panel presents a scan at smaller incommensurability, and the picture here is clearly quite different. There is a conspicuous satellite line below the *C*-phase position, and the peak is substantially weaker and broader. The smooth curve is a least-squares fit to two power-averaged Lorentzians with equal halfwidths of 0.0041 Å^{-1} centered about $Q_{\text{comm}}+\epsilon$ and $Q_{\text{comm}}-\epsilon/2$, with $\epsilon=0.0306$ Å^{-1}. This model clearly does not describe the data nearly as well as the floating-solid model for the scan in Fig. 8(a). The satellite line has been discussed before as a consequence of strain modulation of the adsorbate by the substrate.[16,17] We will discuss its location and intensity later in this section.

Heiney *et al.* have noted that, for small exponent η, a Lorentzian

$$\frac{d\sigma(\vec{Q})}{d\Omega} \propto \frac{1}{\kappa^2+|\vec{Q}-\vec{\tau}|^2},$$

with κ on the order of $1/L$, also fits the power-law line shape over a limited range of wave vectors near the Bragg peak.[28] Indeed, a Lorentzian fit to the scan in Fig. 8(a) is virtually indistinguishable from the power-law fit shown. However, the Lorentzian in the lower panel is some 8 times broader. A Lorentzian line shape comes from a correlation function

$$\langle \vec{U}_\tau(\vec{r}),\vec{U}(\vec{0})\rangle \propto r^{-1/2}\exp(-\kappa r)$$

in 2D. Therefore, if the Lorentzian model is taken literally, it represents a phase with exponential decay of correlations on a length scale of 250 Å: substantially shorter than the maximum observed crystallite size of 1900 Å in this system, but far larger than conventional fluids which typically have correlation lengths on the order of a few atoms.

Figure 9 shows a sequence of closed-cell-II scans displaying the evolution of the *IC* line shape. The dashed lines are least-squares fits to 2D Lorentzians over the range 1.55–1.8 Å^{-1}. This sequence of scans clearly shows that as the system approaches the *C*-*IC*T from the *IC*-phase side, the main peak broadens as it moves toward the *C*-phase wave vector, the peak intensity drops, and the satellite grows. The fits are good but not exact, particularly in comparison to the quality of the fits for the *C*-phase scans (Figs. 4 and 6), the saturated incommensurate scan [Fig. 8(a)], and the Xe melting results.[28] Nevertheless, in view of the simplicity of the model, we regard the fits as being qualitatively successful. There is clearly a pressing need for the theoretical descriptions of this transition to be extended to the prediction of scattering profiles.

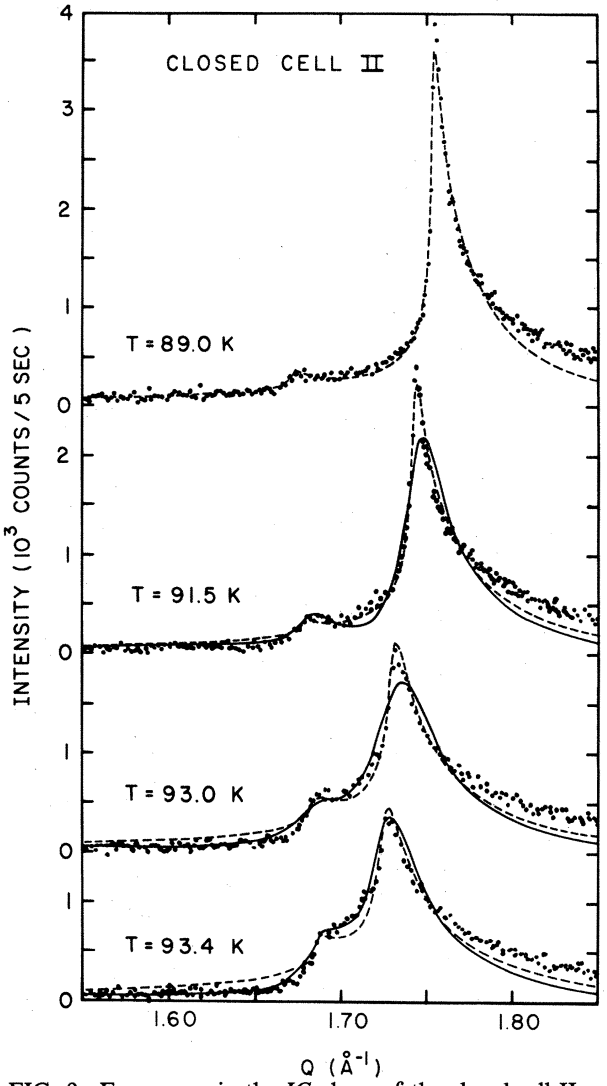

FIG. 9. Four scans in the *IC* phase of the closed-cell-II run. The dashed lines are fits to Lorentzian line shapes; the solid lines are Lorentzian-squared.

It is evident that the experimental scans show considerable excess scattering on the high-Q side of the main peak compared with the prediction of the Lorentzian model. This scattering could either be intrinsic to the adsorbed phase, or arise from small 3D clusters of Kr, condensed in the sample due to capilliary effects. Models discussed below, which ignore the liquidlike disorder of the system, predict a second satellite above the main peak at $Q_{\text{comm}}+5\epsilon/2$, with an integrated intensity comparable to the $Q_{\text{comm}}-\epsilon/2$ peak. As pointed out by D. Fisher,[40] the effect of thermal fluctuations would be to broaden this peak relative to the main peak and the low-Q satellite. This could account for some excess scattering above the main peak. Alternatively, Specht *et al.* have studied the excess high-Q scattering from Kr monolayers at higher temperatures and found that it peaks at the position of the first peak in the 3D liquid-Kr structure factor.[41] This suggests that the excess scattering above the peak arises from bulk liquid Kr, possibly condensed in corners where the graphite crystallites meet. In addition, the Lorentzian model does not fall off as rapidly as the experimental data

for wave vectors below the $Q_{\text{comm}}-\epsilon/2$ satellite. The least-squares-fitted value of κ is therefore a compromise between the intensity of the low-Q wing, which tends to favor small values of κ, and the region between the peaks, which would tend to increase κ in order to raise the intensity in this region toward the experimental value. Nevertheless, the general good fit for the main part of the peak region suggests that κ is well determined.

We have also performed a limited number of fits for two other line-shape models. The first of these is the square of a Lorentzian,

$$\frac{d\sigma(\vec{Q})}{d\Omega} \propto \frac{I_0\kappa^2}{(\kappa^2+|\vec{Q}-\vec{\tau}|^2)^2} .$$

For a given halfwidth, this functional form drops faster in the wing than a Lorentzian. Not surprisingly, this model is able to fit the 93.0- and 93.4-K scans in Fig. 9 (solid lines) slightly better than a Lorentzian; however, it leads to much worse fits for the sharper peaks ($T \leq 92.0$ K). For the parameters of the fits shown, the powder-averaged Lorentzian-squared cross section is essentially zero below 1.65 Å^{-1}. We have therefore adjusted the background in order to enable the model to fit the far wing.

A Lorentzian-squared cross section for this system is motivated by the following argument. An impurity on the graphite surface can act as a local pinning site for the *IC*-phase Kr density wave. Near the *C*-*IC*T, the Kr layer can be expected to be highly susceptible to such pinning. This situation is directly analogous to the problem of random magnetic fields which pin the local spin direction in a magnet. Recent work on the random-field problem has shown that the structure factor of the quasiordered state is a Lorentzian squared.[42] Unfortunately, the data of Fig. 9 do not clearly favor either the Lorentzian or the Lorentzian-squared cross section very near T_c. Consequently, we are unable to conclude whether substrate randomness is important in determining the experimental line shapes in the immediate neighborhood of the transition. Further below T_c the main-peak lineshape is clearly better described by a Lorentzian than a Lorentzian-squared profile.

In an alternative attempt to parametrize the shape of the wing, we inserted a q^4 cutoff term in a Lorentzian. Such a functional form is necessary to describe the transverse correlations in smectic liquid crystals.[43] Hence,

$$\frac{d\sigma(\vec{Q})}{d\Omega} \propto \frac{I_0}{\kappa^2+|\vec{Q}-\vec{\tau}|^2+C_4|\vec{Q}-\vec{\tau}|^4/\kappa^2} .$$

This form does not yield a significant improvement over the Lorentzian or Lorentzian-squared models. Indeed, for scans with $T<92.5$ K, fits to this model converge to vanishingly small values of C_4, thus indicating the preference of a pure Lorentzian cross section for misfits greater than approximately 2%. In short, none of the line-shape models that we have considered provides a completely satisfactory fit to the experimental data throughout the *IC* phase, although the Lorentzian is best overall.

The peak shift ϵ, inverse correlation length κ, and integrated intensity from the series of Lorentzian fits are plotted in Fig. 10. The integrated intensity of a Lorentzian over the full 2D reciprocal space,

$$2\pi\int_0^\infty dq \frac{qI_0}{\kappa^2+q^2} ,$$

diverges. However, within one Brillouin zone, the integral is approximately equal to

$$\pi I_0 \ln(\kappa/2\tau) ,$$

where τ is the wave vector of the first Bragg peak. Over the range of κ in Fig. 10, the logarithm changes negligibly; we may therefore regard I_0 as the integrated intensity. From Fig. 10 one observes that as the peak approaches the *C*-phase position ($T\rightarrow 94$ K), κ grows smoothly, the main-peak integrated intensity remains roughly constant, and the satellite strengthens. The large-error bars for the satellite intensity are systematic due to strong correlations between fitting parameters, uncertainty of background normalization, and the fact that the satellite is sitting on a considerable wing from the main peak. It should be emphasized that the ultimate decrease in κ as one approaches T_c observed in our original synchrotron measurements,[23] and more recently by Specht *et al.*, is not observable here due to the smearing of T_c.

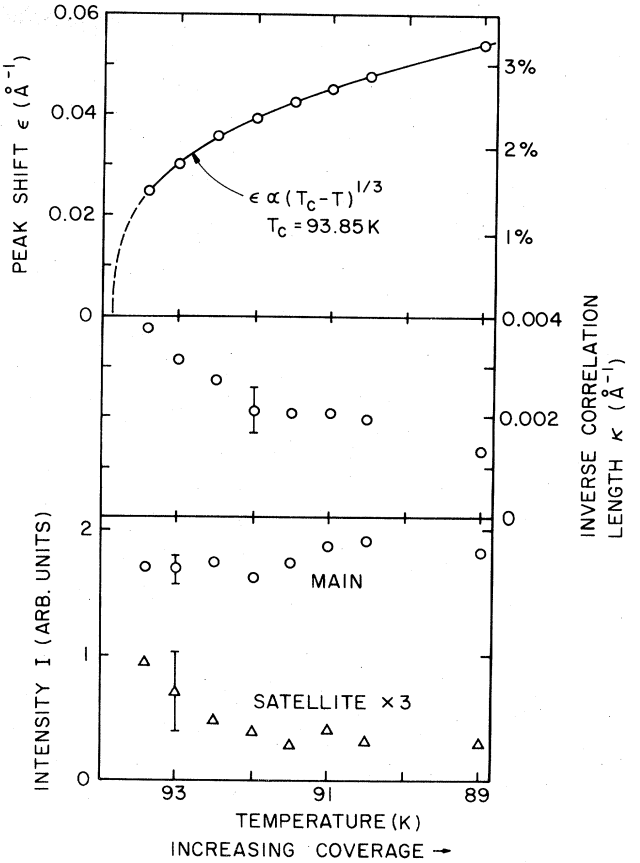

FIG. 10. Parameters of closed-cell-II scans in the *IC* phase fitted to Lorentzian line-shape models.

As discussed in Sec. II, in previous work the peak shift ϵ has been found to depend on the chemical-potential difference $\mu-\mu_c$, according to the simple power-law form of Eq. (1). According to universality, in these closed-cell

scans, one would expect $\epsilon \propto (T_c - T)^{0.33}$. A simple estimate shows that crossover to Fisher-renormalized exponents should be unobservable. The ϵ-vs-T data from the closed-cell-II scan were fit to a power-law form with β fixed at $\frac{1}{3}$, while T_c and the amplitude varied. The result is shown in Fig. 10. While the lack of credible data below a 1.5% misfit precludes the determination of the exponent β from these data, they are clearly consistent with earlier results. T_c from this fit is 93.85 K, which is in the middle of the region of composite line shapes. The $\frac{1}{3}$ power law as a function of T was also observed in the closed-cell-I scans.[23]

Figure 11 shows a similar evolution of the parameters in the constant-temperature scan. Here again, we have checked the power-law dependence of ϵ on $\mu - \mu_c$. The fact that the vapor pressure was measured allows us to determine the amplitude A as well. The solid line shows a fit to Eq. (1) with the exponent β fixed at $\frac{1}{3}$, and with the critical pressure P_c and the amplitude A varied. The resulting parameters are $P_c = 3.21$ Torr and $A = 0.0134$ Å^{-1}, consistent with the previous value. Using this value of P_c, we have also plotted the results of these scans in Fig. 1 for direct comparison with earlier results.

We next discuss the *IC*-phase measurements in the closed-cell-I experiment. Figure 12 shows six scans with fits to Lorentzian and Lorentzian-squared line-shape models. It is clear there is no trace of a sharp *C*-phase peak coexisting with the *IC*-phase scans. Specifically, the 97.06-, 97.18-, and 97.24-K scans all have incommensurability smaller than 0.022 Å^{-1}, the smallest value for ϵ observed in a single-phase *IC*-phase scan in either the closed-cell-II or constant-temperature data. This provides additional evidence that the composite structure observed in the two later runs is not an intrinsic feature of the *C-IC*T in this range of ϵ. The poor statistics and uncertainty of the background correction make it impossible to state with any confidence that either model provides a more accurate description of the profiles in Fig. 12.

The two bottom scans in Fig. 12 show only one peak, at $Q_{\text{comm}} + \epsilon$. If a second peak at $Q_{\text{comm}} - \epsilon/2$ is added, the least-squares fit actually converges to a slightly negative value for the satellite amplitude. Again this result is dependent upon the background correction, and so we do not attach great significance to it. As we discuss below,

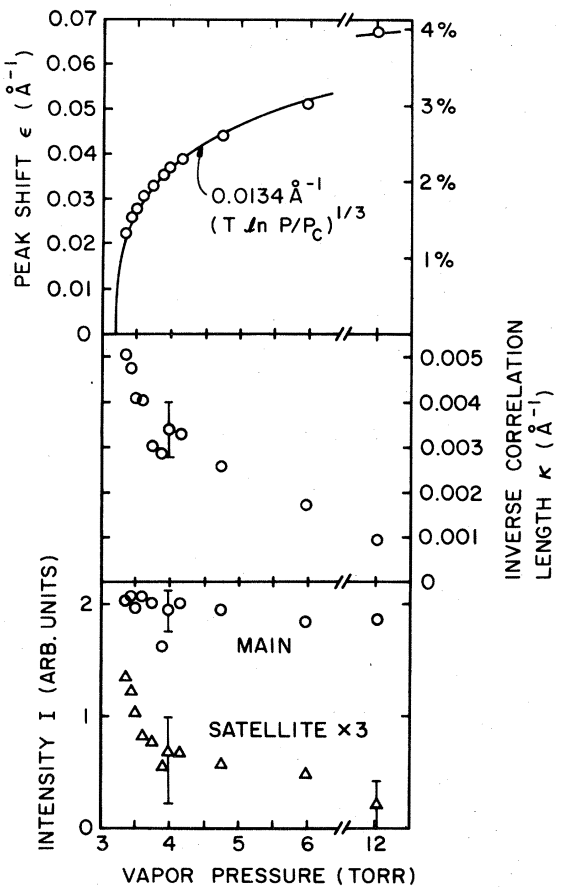

FIG. 11. Parameters of constant-temperature scans in the *IC* phase fitted to Lorentzian line-shape models.

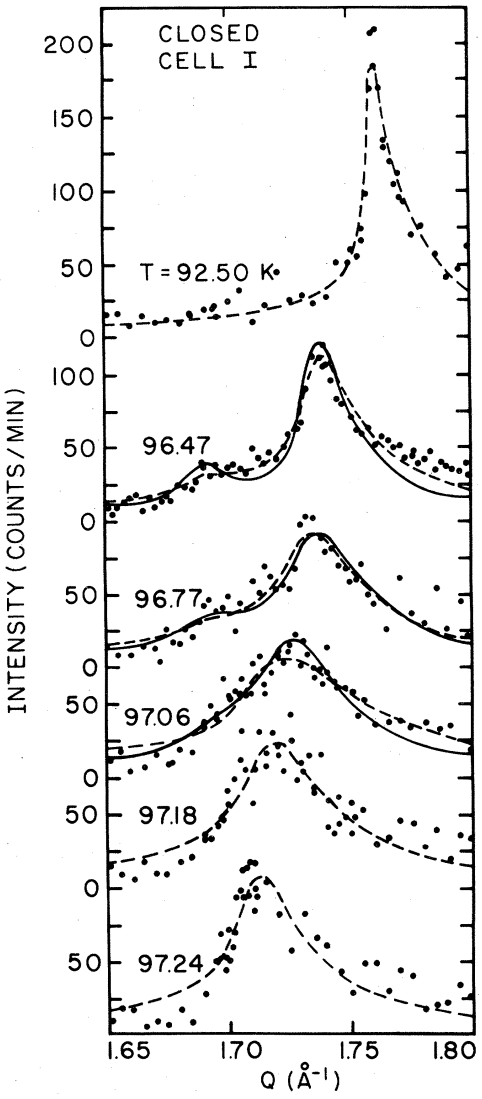

FIG. 12. Closed-cell-I scans in the *IC* phase. The dashed lines are fits to powder-averaged Lorentzian line shapes, and the solid lines are Lorentzian-squared. The 96.47-K scan was counted for 4 min/point. The 92.05-, 97.18-, and 97.24-K scans are fitted to a single Lorentzian.

for a rigid domain-wall lattice, the amplitude of the $Q_{\text{comm}}-\epsilon/2$ peak is expected to grow continuously with decreasing incommensurability. This rather surprising result therefore requires further study.

In the previous communication of the closed-cell-I results,[23] we showed that at small incommensurability the ratio ϵ/κ of peak shift to peak halfwidth was on the order of unity for small ϵ (below ~ 0.02 Å^{-1}). Figure 13 shows this ratio for all three runs. Unfortunately, the higher statistics closed-cell-II and constant-temperature runs do not reach a sufficiently small ϵ to study this issue further. However, they do show the same trend of ϵ/κ increasing very quickly for $\epsilon > 0.02$ Å^{-1}. The apparent systematic disagreement between the data sets may well be due to the absence of a baseline below 1.65 Å^{-1} in the closed-cell-I scans.

One of the most interesting features of Fig. 13 is that at the smallest values of ϵ studied, the peak width κ is on the order of its incommensurability ϵ. In the case of an ordered array of hexagonal domain walls separated by a distance of l, the main diffraction peak appears at a value of $\epsilon = 4\pi/3l$. Taking the correlation length L to be $1/\kappa$, we see that the small ϵ value of $\epsilon/\kappa \sim 1$ implies that $L \sim l/4$. Thus within a small numerical factor, the domain walls are disordered on the length scale of their separation.

We conclude this section with an analysis of the satellite peak, observable in Figs. 3, 8(b), and 9 at $Q_{\text{comm}}-\epsilon/2$. The position and intensity of this peak gives information about the structure of the *IC* phase. We shall discuss it using both domain-wall and continuous-strain-modulation descriptions of the *IC* phase. At the outset, it is important to note that these models are based on an adsorbate with long-range order, and are therefore expected to have only limited validity for the case of weakly *IC*-phase Kr.

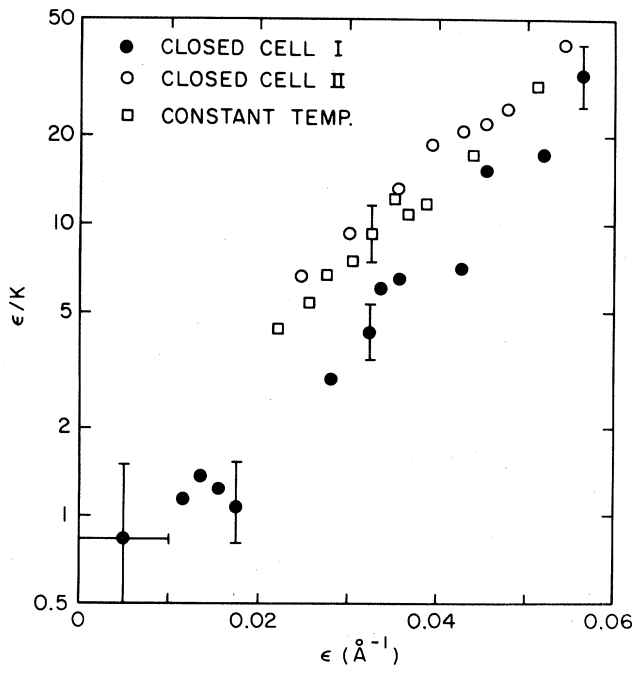

FIG. 13. Ratio of peak shift to peak width as a function of peak shift for three data sets.

We discuss the consequences of the absence of long-range order at the end of this section.

As discussed in the Introduction, a weakly *IC* phase is frequently described as a superlattice of *C*-phase regions, separated by a regular network of domain walls. It is straightforward to calculate the diffraction pattern of such a superlattice for an assumed pattern of domain walls.[16,44] Because the superlattice translation vector is much less than that of the *C*-phase lattice, the density of reciprocal-lattice points is much higher. However, only diffraction peaks close to the original *C*-phase spots have a significant intensity. Increasing the size of the superlattice reduces the mesh of the reciprocal lattice, so that the strong diffraction peaks move closer to the *C*-phase position.

Figure 14 shows three hexagonal domain arrays with their strongest diffraction spots indicated. In all three cases, the domain walls are oriented along the graphite $\langle 110 \rangle$ directions. Because the superlattice translation vector is not an integer multiple of the *C*-phase overlayer translation, the *C*-phase diffraction peak is *not* allowed in the *IC*-phase pattern.

The pattern in Fig. 14(a) is produced by moving hexagonal arrays of atoms closer by one graphite-substrate lattice vector. The corresponding diffraction pattern consists of three peaks of equal intensity about each *C*-phase location. A powder pattern of this phase would consist of a peak at $Q_{\text{comm}}-\epsilon$ and a second peak, of twice the intensity, at $Q_{\text{comm}}+\epsilon/2$. On the other hand, if the hexagons are moved apart as in Fig. 14(b), the powder pattern gives peaks at $Q_{\text{comm}}+\epsilon$ and $Q_{\text{comm}}-\epsilon/2$, as observed in the present experiments. The center of mass, however, still does not move from the *C*-phase diffraction-peak position. If a row of interstitials is added to the light wall structure (producing a superheavy wall in the nonenclature of Kardar and Berker[9]), the $Q_{\text{comm}}+\epsilon$ peak grows stronger while the two $Q_{\text{comm}}-\epsilon/2$ peaks weaken [Fig. 14(c)]. In addition, a peak at $Q_{\text{comm}}+5\epsilon/2$ begins to appear.[44] Finally, we note that if the atoms in a compressed *IC* phase relax towards the nearest $(\sqrt{3}\times\sqrt{3})R30°$ site, the superheavy-wall configuration of Fig. 14(c) is obtained.

This description of atoms pinned to adsorption sites is not directly applicable to physiadsorbed monolayers because of the relatively weak site specificity. Accordingly, one has to imagine a broad domain wall. For the purposes of a specific calculation, we divide each locally *C*-phase domain into hexagonal shells, and uniformly shrink the nth shell, counting inward from the row of interstitials so that its longitudinal motion is $[1-\tanh(n/\lambda)]/2$ substrate sites, where λ, the width of the wall, is an adjustable parameter. The interstitial row can therefore be thought of as a zeroth layer of atoms contracted by a $\frac{1}{2}$ substrate site. The inset of Fig. 15 shows the intensity of the three most prominent lines as a function of λ for a particular superlattice size (superlattice translation vector equal to 28 graphite sites, giving $\epsilon = 0.041$ Å^{-1}).

If the parameter λ is fixed, the satellite lines get weaker when the domain walls are brought closer together and the adsorbate approaches the limit of uniform compression. Figure 15 compares the predicted evolution of intensity for $\lambda = 5.7$ with the data from the fits of Figs. 10 and 11

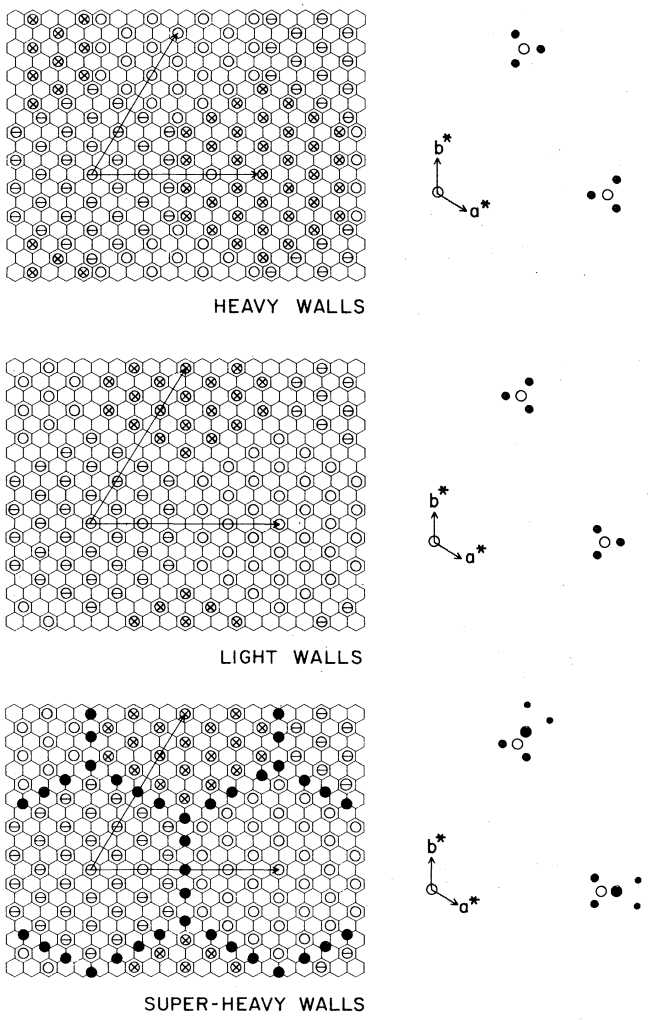

FIG. 14. Hexagonal domain structures (left) and corresponding reciprocal lattices (right). Atoms on the three sublattices are shown by different symbols, with atoms on the saddles or peaks drawn as solid circles. The arrows are superlattice translation vectors. On the reciprocal lattices, only peaks with an intensity greater than 1% of the strongest peak are shown. Open circles indicate *C*-phase peak position. The size of the symbol roughly indicates the intensity of the corresponding peak. Note that the superheavy wall is made up of a light wall with added rows of interstitial atoms between the *C* domains. The heavy- and superheavy-wall configurations are identical to cases *b* and *a*, respectively, in Fig.2 of Ref. 44.

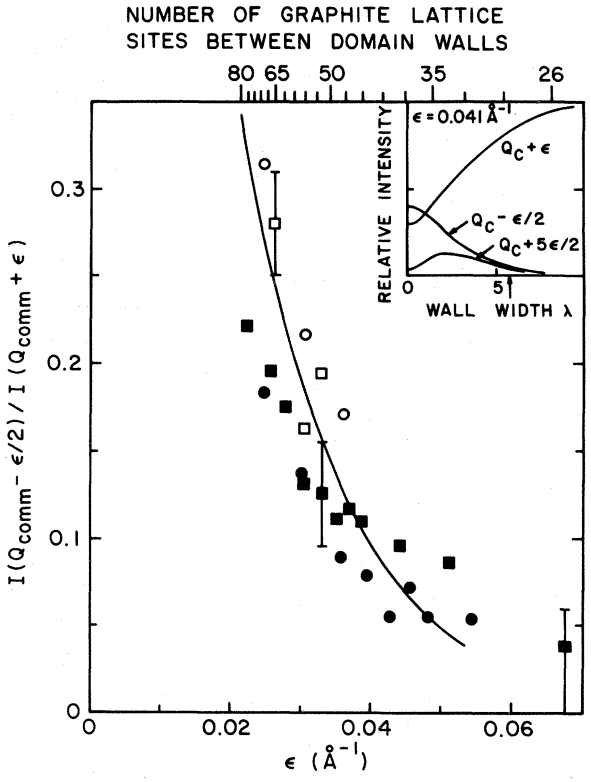

FIG. 15. Ratio of $Q_{\rm comm}-\epsilon/2$ to $Q_{\rm comm}+\epsilon$ intensities vs misfit ϵ. Solid symbols are from fits to Lorentzian models, and open symbols are Lorentzian-squared. The circles represent data from the closed-cell-II scans, and the squares are from the constant-temperature run. The smooth curve was calculated from domain lattice diffraction patterns for superheavy walls with width $\lambda=5.7$ rows of Kr atoms. Inset shows the relative intensities in a powder pattern of the three strongest reflections for an array of superheavy walls as a function of λ for incommensurability $\epsilon=0.041$ Å^{-1}. The arrow shows the value of λ used for the solid line in the main figure.

to the Lorentzian model (solid symbols) and to fits to Lorentzian-squared model (open symbols). The general trend is correct, with systematic differences between the different line-shape models contributing the major source of uncertainty in this measurement. The scatter of the data admits a variation of ±1 in λ. Alternative wall-relaxation models (exponential and linear) give similar results. For wall widths λ on the order of the observed value, the inset of Fig. 15 shows that the $Q_{\rm comm}+5\epsilon/2$ peak intensity should be comparable to that of the $Q_{\rm comm}-\epsilon/2$ satellite. The fact that no sharp peak is observed at this wave vector is obviously a major failing of the rigid domain-wall model.

An alternative description of the static structure of the strain modulation in the *IC* phase considers the adsorbate to be a solid with reciprocal lattice (τ) whose atoms are displaced by a weak elastic interaction with the substrate. The atom which would be at a position $\vec{R}$ in the unstrained adsorbate is moved to a position $\vec{R}+\vec{U}(\vec{R})$. Expanding $\vec{U}(\vec{R})$ in a Fourier series in substrate reciprocal-lattice vectors $\{\vec{G}\}$ and retaining terms only to lowest order in the displacement amplitudes gives a result for the scattering cross section on a single infinitely large crystallite,[45]

$$|S(\vec{K})|^2 \propto \sum_{\{\vec{\tau}\}} \delta(\vec{K}-\vec{\tau}) + \sum_{\{\vec{\tau}\}}\sum_{\{\vec{G}\}} [\vec{K}\cdot\vec{U}(\vec{G})]^2 \delta(\vec{K}-\vec{\tau}-\vec{G}) , \quad (6)$$

where

$$\vec{U}(\vec{R}) = \sum_{\{\vec{G}\}} e^{i\vec{G}\cdot\vec{U}(\vec{R})} .$$

Clearly, the domain-wall description is equivalent to this expansion [though not the small displacement limit in (6)] if the coefficients $\{\vec{U}(\vec{G})\}$ are known for a particular domain-wall configuration. The opposite limit, of a sinusoidal modulation, is obtained by considering only the longest-wavelength nonzero contributions to $\vec{U}(\vec{G})$. This is a triple-q structure because the six equivalent graphite $\{100\}$ wave vectors contribute equally. Sinusoidal modulation of an unrotated adsorbate therefore gives six modulation spots around each adsorbate diffraction vector $\vec{\tau}$. Figure 16(a) shows the geometry appropriate to a compressed $(\sqrt{3}\times\sqrt{3})R30°$ monolayer. If τ is increased from its C-phase value $Q_{\rm comm}=|\vec{G}|/\sqrt{3}$ by a small amount ϵ, satellites will be seen in a powder pattern at $Q_{\rm comm}-\epsilon/2$, $Q_{\rm comm}+\epsilon$, and $Q_{\rm comm}+5\epsilon/2$. If the adsorbate is unrotated, the distortions will be longitudinal, i.e., $\vec{U}(\vec{G})$ will be parallel to $\vec{G}$. Then the $Q_{\rm comm}-\epsilon/2$ and $Q_{\rm comm}+5\epsilon/2$ satellites will have equal intensities and the $Q_{\rm comm}+\epsilon$ satellite will have zero intensity. (In any event, the $Q_{\rm comm}+\epsilon$ satellite is unobservable in a powder because it is nearly degenerate with τ.)

Again, the relative intensity of main and staellite peaks allows us to estimate the atomic displacements. From Eq. (6) we see that in a powder pattern the ratio of peak intensities

$$\frac{I(Q_{\rm comm}-\epsilon/2)}{I(Q_{\rm comm}+\epsilon)}=2\{\vec{K}\cdot\vec{U}([100])\}^2\,, \tag{7}$$

where the factor of 2 arises from the degeneracy of the satellite peak. Using the intensities of the $Q_{\rm comm}-\epsilon/2$ and $Q_{\rm comm}+\epsilon$ peaks and assuming that $\vec{U}\|\vec{G}$, we find that the amplitude of each of the three triple-q displacement waves varies from 0.25 Å for the most prominent satellites to 0.1 Å at the largest incommensurabilities studied.

Both the domain-wall and the sinusoidal-modulation descriptions predict that in the weakly *IC*-phase hexagonal phase a powder pattern should have a main diffraction peak surrounded by two satellites of equal intensities. No scan that we have measured has ever shown such a sharp satellite line on the high-Q side. The fact that neither model accounts for this absence prevents us from distinguishing between the domain-wall and sinusoidal-modulation descriptions on this basis. Indeed, these experiments provide no direct evidence in favor of the domain-wall picture of the weakly *IC* phase.

The models discussed above have not taken disorder into account. D. Fisher has pointed out that the $Q_{\rm comm}+5\epsilon/2$ peak is generated by a higher-order Kr reflection than the main *IC*-phase peak or the $Q_{\rm comm}-\epsilon/2$ [see Fig. 16(a)].[40] Because the weakly *IC* phase is disordered, the Kr(2 1) peak, occurring at a wave vector $\sqrt{7}\tau_{(10)}$ is expected to be considerably broader and weaker than the Kr(1 0) peak. Indeed, all of the scans in Fig. 9 have an excess intensity on the high-wave-vector side of the principal peak, which might be attributed to this effect. Uncertainties in the background and graphite vertical mosaic, as well as possible interference with the graphite (002) peak and traces of 3D Kr, preclude a quantitative analysis of the possible $Q_{\rm comm}+5\epsilon/2$ satellite intensity.

As discussed in the Introduction, one scenario for this transition calls for an intervening uniaxially compressed phase;[2] it is therefore of interest to determine the diffraction signal expected from such a phase. If the compression is in a graphite [100] direction (so that the domain walls run in graphite [110] directions as in the hexagonal case), then Fig. 16(b) shows that there will be diffraction peaks at $Q_{\rm comm}+\epsilon$ and $Q_{\rm comm}+\epsilon/4$ in the ratio of 1 to 2. On the other hand, if the compression is in the [110] direction, one, peak remains at the C-phase location while another, of double intensity, shifts to higher wave vector [Fig. 16(c)]. In either case, strain-modulation satellites will appear, but they do not alter the fact that in a uniaxially compressed phase, there will be two adsorbate diffraction peaks with intensities in the ratio of 2 to 1. Direct computations in the sharp domain-wall limit for the uniaxially compressed case agree with this conclusion.[39] Since this signature is not present in any of our diffraction patterns, we conclude that there is no evidence for a uniaxially compressed *IC* phase in this system.

In conclusion, we can understand the satellite peak either as arising from a hexagonal array of superheavy domain walls with a width of a few Kr lattice rows, or as a consequence of a triple-q sinusoidal modulation, from the graphite substrate. For a phase with long-range order, an additional satellite should be present at $Q_{\rm comm}+5\epsilon/2$.

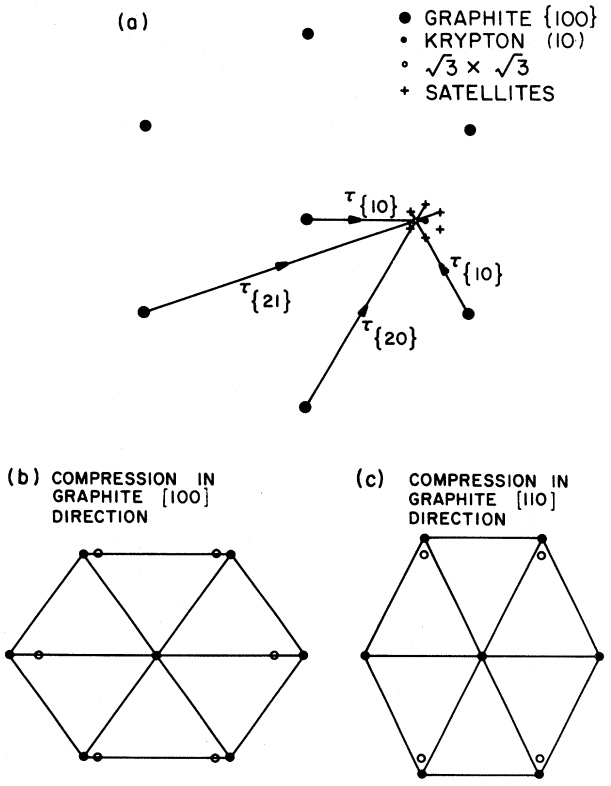

FIG. 16. (a) Reciprocal lattice showing source of graphite modulation satellites around Kr(1 0) diffraction peak for a uniformly compressed overlayer. (b) Motion of $\sqrt{3}\times\sqrt{3}$ Kr peaks for uniaxial compression in a graphite [100] direction. (c) Motion of $\sqrt{3}\times\sqrt{3}$ Kr peaks for uniaxial compression in a graphite [110] direction. The bottom two panels do not show modulation satellites, only the main Kr reflections.

However, because the satellite is only observed in the disordered *IC* phase, a high-Q satellite would be expected to be much broader than the other peaks, rendering it unobservable. Finally, there is no striped phase at the limit of the resolution of these experiments.

VI. TRANSITION REGION

In the preceding two sections, we have discussed the scans which are either in the *C* or the *IC* phase. There is a narrow region in the more recent experiment with a composite line shape having *C*- and *IC*-phase peaks. This was observed in both the closed-cell-II and the constant-temperature data sets. In general, a composite line could arise either from coexistence in a first-order phase transition between *C* and *IC* phases, or from a rounded transition. However, in order to explain the finite coexistence range in the constant-temperature scans, pronounced rounding is required since a sharp first-order transition in the adsorbate would manifest itself as a discontinuous jump from the *C* to *IC* phase as the bulk vapor pressure was varied. Correspondingly it is clear that this rounding phenomenon has an important effect on the line shapes observed in the immediate neighborhood of the *C*-*IC*T.[46]

Figure 17 shows a series of scans at fixed temperature, spanning this composite line-shape domain. In order to test for possible two-phase coexistence, we have fitted each scan as the sum of the two extremal line shapes. The smooth curves in Fig. 17 show these best fits. These are not specific line-shape models, but rather are point-by-point sums of the experimental scans at 3.06 and 3.35 Torr. In the case of coexistence in a first-order transition, the composite line shapes would be a direct sum of the two extremal forms. The three middle scans in Fig. 17, 3.20, 3.22, and 3.25 Torr, all have significant deviations ($x^2=4.7$, 5.3, and 4.2; two parameters) from this simple coexistence model. Specifically, they show an excess of scattering between the two archetypal peak positions. It is therefore clear that these scans show a continuously evolving *IC*-phase line profile plus a decreasing *C*-phase peak, as the vapor pressure is increased, as one would expect for a rounded transition. We emphasize that the poor agreement with the three intermediate scans does not imply that the rounding hypothesis is incorrect, but rather that the 3.35-Torr scan does not show the smallest nonzero incommensurability in this sample. While the smeared transition precludes a direct determination of the minimum incommensurability in this sample, the excess scattering around 1.71 Å^{-1} in Fig. 17 clearly shows that the median misfit ϵ is less than the 0.022 Å^{-1} of the 3.35-Torr scan; qualitatively, the *IC*-phase data are consistent with the closed-cell-I results where the rounding was much less severe. Specifically, from Figs. 6 and 12, it is evident that in the earlier closed-cell-I data set there is no trace of coexisting *C* and *IC* phases. Because the statistics of the closed-cell-I scan are so poor, we cannot preclude a 1% first-order jump.

We do not know, with certainty, the origin of the rounding in the more recent experiments. The most likely cause is simply, that the sample used for the 1981 run became contaminated in the year between the time it was baked and used. The same substrate was used in the Xe melting experiment of Ref. 28. This latter work had no evidence of coexistence at 1.1 monolayers. However, the measured liquid correlation length shows rounding behavior above $\sim$200 Å. It is also impossible to exclude a first-order melting transiton to a liquid with a correlation length larger than 200 Å in the Xe work. For comparison, the separation of domain walls in an ordered hexagonal array with peak shift ϵ is $l=4\pi/3\epsilon$, which is equal to 190 Å for the 3.35-Torr scan, the smallest incommensurability observed without a coexisting *C*-phase line. The fact that these two different experimental systems, the *C*-

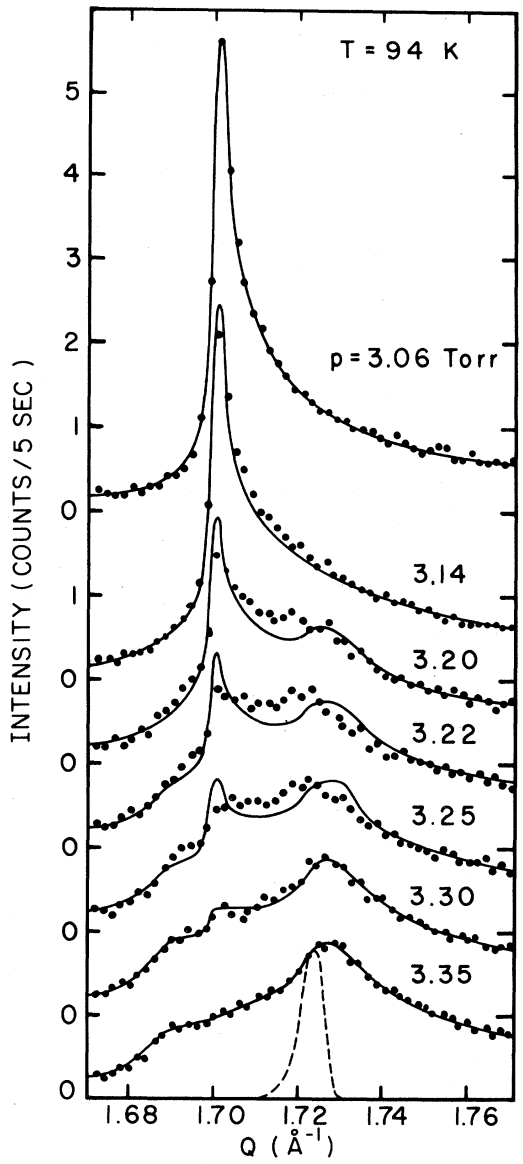

FIG. 17. Scans spanning the apparent coexistence range of the constant-temperature data set. The smooth curves between 3.14 and 3.30 Torr, inclusive, represent sums of the 3.06- and 3.35-Torr scans, with the relative weights adjusted to give the least-squares fit. The dashed line represents the distribution of incommensurabilities derived from the inhomogeneous broadening model discussed in the text.

*IC*T of Kr and the melting of the *IC*-phase Xe, have comparable length scales for rounding suggests that the same mechanism is responsible in both cases. As noted in the section on line-shape analysis, impurities on the surface enter this problem in the manner of a random field. If such effects are important then one would expect Lorentzian-squared profiles very near the *C*-*IC*T. In fact, as discussed previously, the Lorentzian-squared fits are quite good at very small incommmensurabilities. However, a systematic study as a function of surface impurity concentration would be necessary to establish this effect definitively. Steps on the substrate will be less significant as a source of rounding because of their large separation (1900 Å).

We establish upper limits on the widths of the distribution of critical points as follows. From the data of Fig. 17, the relative *C*-phase intensity is 0.74 at 3.14 Torr and 0.26 at 3.22 Torr. A Gaussian distribution of critical pressures would produce a *C*-phase intensity proportional to an error function. Using the values above, we find a mean critical pressure at 3.18 Torr and a HWHM of 0.07 Torr. An equivalent analysis of the closed-cell-II data based on the *C*-phase intensity from Fig. 7(b) leads to a rounding in temperature of 0.24 K HWHM. For the closed-cell-I data of Fig. 7(a), no coexistence was observed; however, we may establish an upper limit of 0.20 K HWHM. Indeed all of these numbers are upper limits because they ignore any intrinsic evolution of the line shape as critical scattering near melting.

This distribution of critical pressures will contribute an inhomogeneous broadening to the *IC*-phase line shape, because one particular vapor pressure will produce diffraction lines at different incommensurabilities.[46] In order to assess the importance of this mechanism in producing the observed broad *IC*-phase lines, we argue as follows: At some given temperature T, suppose that the distribution $P(\mu_c)$ of critical chemical potentials is Gaussian about μ_{c0} with HWHM of $(\ln 2)^{1/2}\Delta\mu_c$, i.e.,

$$P(\mu_c)=\Delta\mu_c^{-1}\pi^{-1/2}\exp\{[(\mu_c-\mu_{c0})/\Delta\mu_c]^2\} .$$

Then the fraction of crystallites in the *C* phase is

$$\tfrac{1}{2}\{1-\mathrm{erf}[(\mu-\mu_{c0})/\Delta\mu_c]\} .$$

Inserting Eq. (1), we see that for a specified chemical potential μ the probability density for misfit ϵ is given by

$$P(\epsilon)=\frac{3\epsilon^2}{\Delta\mu_c\pi^{1/2}A^3}\exp\left[-\left[\frac{\mu-\mu_{c0}-(\epsilon/A)^3}{\Delta\mu_c}\right]^2\right] +\frac{1}{2}\left[1-\mathrm{erf}\left[\frac{\mu-\mu_{c0}}{\Delta\mu_c}\right]\right]\delta(\epsilon) . \quad (8)$$

Taking the experimental value of $A=0.0134$ Å^{-1} and the estimate f $\Delta\mu_c=(94\text{ K})(0.09\text{ Torr})/(3.18\text{ Torr})=2.6$ K discussed above for the constant-temperature data, one obtains the probability density shown in Fig. 18. These are not model line shapes; they do not contain the sample-size-limited diffraction peak width, vertical mosaic, strain-modulation satellites, or phonon wings. It is important to note that because the distribution of incommensurabilities vanishes near $\epsilon=0$, the scattered intensity

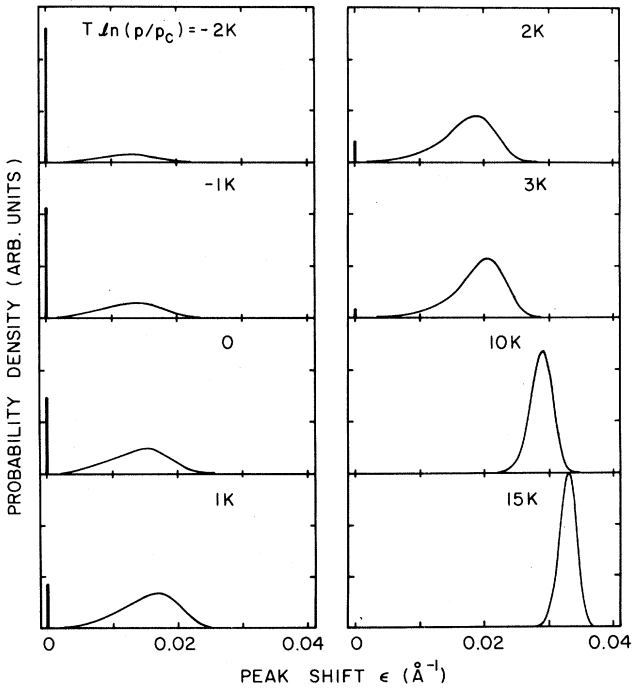

FIG. 18. Probability density of misfit ϵ based on a Gaussian distribution of critical points as discussed in the text. The heavy vertical lines at $\epsilon=0$ represent the $\delta(\epsilon)$ term as the peak height of a Gaussian with HWHM of 0.0016 Å^{-1}, as appropriate for the *C*-phase peak. The distribution of critical chemical potentials has HWHM of 2.1 K.

peaks at finite ϵ. The minimum observed peak shift ϵ under these circumstances will be on the order of $A(\Delta\mu)^\beta$, 0.018 Å^{-1} in the present experiment. This is consistent with the position of the peaks of the (3.20—3.25)-Torr scans in Fig. 17.

We now compare the width of the inhomogeneously broadened distribution of ϵ with the experimental line shapes outside of the composite domain. The dashed line in Fig. 17 shows the distribution expected for $T\ln(P/P_c)=5$ K, appropriate to the 3.35-Torr scan. It is clear that the calculated distribution of ϵ is significantly narrower than the observed line shape. At $T\ln(P/P)_c=15$ K, shown in Fig. 18, we see that the distribution of ϵ has HWHM 0.0016 Å^{-1}, identical to the width of the *C*-phase scans. This may be compared with the 93.0-K closed-cell-II scan in Fig. 9 or the 96.47-K closed-cell-I scan in Fig. 12, both of which exhibit peaks which are very much broader than the *C*-phase Bragg profiles. Finally, the last panel of Fig. 18 shows that the expected distribution is nearly Gaussian, in contrast to the broad wings experimentally observed for scans in this range of incommensurability.

VII. FINAL OBSERVATIONS

In the preceding sections, we have shown that the *C*-*IC*T in a Kr monolayer on graphite takes place via a phase with a large degree of disorder. Indeed, we believe that this is the most important feature of this transition and that the discussion of any features such as satellite peaks, the functional form of misfit versus driving pres-

sure, or the question of whether the transition is continuous, must be phrased within the context of a system which loses its long-range order in a most dramatic fashion. As discussed in the Introduction, several theoretical accounts of a *C-IC*T based on disorder have appeared since our original discovery of the effect.

One of the most interesting of these theoretical models is that of Huse and Fisher, who suggest that if the asymmetry in the domain-wall energy is large, the *C-IC* T should be a melting transition in a new universality class.[10] Specifically, they predict that the peak in $S(q)$ will move from its *C*-phase value in a critical way: $\epsilon/\kappa=\text{const}\cong O(1)$. Indeed our experiments do show that $\epsilon/\kappa\rightarrow 1$ as the transition is approached from the *IC* phase. However, the temperature dependence of ϵ and κ are different except perhaps in an extremely small region near T_c. Thus the validity of the Huse-Fisher model remains to be tested experimentally.

We close this paper with an observation on the variation of the critical pressure as a function of temperature. The Kr/graphite *C-IC*T has been studied between 52 and 130 K with critical pressures varying by a factor of 5×10^9. Fain *et al.* have fitted critical pressure as a function of temperature by

$$P_c(T)=P_0\exp(-q/T)\ ,$$

with $P_0=4.5\times 10^9$ Torr and $q=1990$ K.[18] However, they are unable to account for the observed constancy of q over a factor of 2.5 in temperature.

We suggest a different functional form for $P_c(T)$ which makes contact with current theories. The *C-IC*T in a monolayer film is driven by the chemical potential of the reservoir of 3D gas in contact with the adsorbate. The chemical potential of a monatomic ideal gas of N atoms of mass m at pressure P and temperature T is given by

$$\mu=kT\ln\left[\frac{P}{kT}\frac{h^3}{(2\pi mkT)^{3/2}}\right]\ , \tag{9}$$

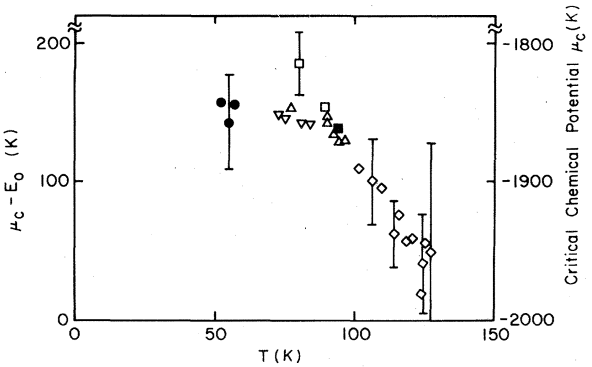

FIG. 19. Comparison of the critical chemical potential μ_c at the *C-IC*T. Solid circles show LEED results, Refs. 15 and 18; upright and inverted triangles show vapor-pressure isotherms, Refs. 14 and 47, respectively; open squares show x-ray diffraction, Ref. 16; solid square shows this work (94.0 K and 3.18 Torr); diamonds show heat capacity, Ref. 24. The error bars below 100 K represent a temperature uncertainty of ± 1 K; on the heat-capacity results, the error bars reflect larger temperature uncertainties due to the width of the heat-capacity peaks.

where k and h are Boltzmann's and Planck's constants, respectively. Figure 19 shows the chemical potential μ_c at the critical point for the data surveyed by Fain *et al.*, together with the present work. μ_c appears to be constant below about 90 K, and decreases with further increase in temperature. It is appropriate to measure μ with respect to the binding energy E_0 of an atom in the *C* phase. If we take the Kr-graphite binding energy as -1466 K (Ref. 48) and the Kr-Kr energy as $3V_{\rm LJ}$ (4.27 Å), where $V_{\rm LJ}$ is the Lennard-Jones potential appropriate to Kr, the binding energy is (-2000 ± 10) K.[49]

Pokrovsky and Talapov[3] have given an expression for the critical chemical potential as a function of T for a one-dimensional *C-IC*T which qualitatively matches Fig. 19. We regard the value of E_0 given above as a crude estimate, and so we are willing only to say that it is very suggestive that the *C* phase disappears when μ_c-E_0 approaches zero. On the other hand, it is interesting to note that below 90 K, μ_c is approximately temperature independent. Therefore over most of the experimental range, the data appear to be in the low-temperature limit insofar as fluctuations are not sufficient to alter μ_c significantly.

As discussed earlier in this paper, the extra entropy in breathing modes of the *HIC* phase may stabilize it relative to the *SIC* phase, leading to a weakly first-order *C-HIC* transition. Using arguments based on the work of Villain,[5] Coppersmith *et al.*[6] have shown that the *C-HIC* transition takes place at a chemical potential which is lower than that at which the *C-SIC* transition would have occurred by an amount on the order of T/l_c where l_c is the number of graphite lattice constants between domain walls at the transition. From Fig. 15 we see that l_c is at least 65 for the data reported here, so that the critical chemical potential for the *C-HIC* transition is expected to be insignificantly reduced from the value calculated for a *SIC* phase. Clearly, there is a need for more accurate measurements of $\mu_c(T)$ at higher temperatures.

ACKNOWLEDGMENTS

We wish to thank A. N. Berker, W. F. Brinkman, D. M. Butler, S. C. Fain, Jr., D. S. Fisher, G. Grinstein, B. I. Halperin, J. P. McTague, and T. M. Rice for many stimulating and useful discussions. We also thank the staff of the Stanford Synchrotron Radiation Laboratory (SSRL) for their helpful assistance. Work at SSRL was supported by the National Science Foundation under Contract No. DMR77-27489 at the Massachusetts Institute of Technology by the U.S. Joint Services Electronics Program under Contract No. DAAG-29-80-C-D109, and by the U.S. Army Research Office under Contract No. DAAG-29-81-K-0029, and at State University of New York, Stony Brook, by the National Science Foundation under Grant No. DMR-820-8570, and the Research Corporation.

APPENDIX: POWDER-AVERAGED LINE SHAPES

Line-shape analysis is an important aspect of this and related work. The asymmetric "sawtooth" shape is

perhaps the most visible consequence of the distribution of orientations of 2D scatterers, but the shape of the leading edge is also affected. The original Warren model[30] and its modifications[31] contain several uncontrolled approximations, and it is not at all clear how they should be extended to other than Gaussian line-shape models. We have derived a general technique for calculating powder-averaged line shapes, which we present here in detail.

Because the adsorbate extends into only two dimensions, there is no constraint on the momentum transferred perpendicular to the layer. The scattering cross section for any given crystallite is extended along a line perpendicular to the crystallite, and therefore contributes to the experimentally measured signal at the wave vector where that line crosses the scattering plane.

We start by describing a given crystallite in terms of its Eulerian angles ω, χ, and ϕ.[50] χ and ω are polar and azimuthal angles defining the crystallite c axis (perpendicular to the layer) relative to the average c-axis direction, and ϕ is the rotation of the crystallite about its c axis. The transform from space axes to body axes is given in Eq. 4-46 of Ref. 51. We choose the scattering wave vector $\vec{Q}$ to be along the space $\hat{X}$ direction and transform it into body axes ($\hat{x}'$, $\hat{y}'$, and $\hat{z}'$) as follows:

$$\begin{aligned}\vec{Q}=Q\hat{x}=&Q(\cos\omega\cos\phi-\sin\omega\cos\chi\sin\phi)\hat{x}'\\&+Q(-\cos\omega\sin\phi-\sin\omega\cos\chi\cos\phi)\hat{y}'\\&+Q(\sin\omega\sin\chi)\hat{z}'\ .\end{aligned}\tag{A1}$$

We limit attention to cases for which the scattering cross section is symmetrical about each zone center, e.g., Gaussian or Lorentzian lines about some given wave vector q_0. The scattered intensity on one crystallite then may be written as

$$I(\vec{Q}')=I([(Q_x'-q_0)^2+Q_y'^2]^{1/2})F(Q'_z)\ ,\tag{A2}$$

where Q_x', Q_y' and Q_z' are wave-vector components on the given crystallite, given by (A1). The $F(Q_z')$ term arises from interplanar correlations in multilayer films.

We next consider the distribution of ω, χ, and ϕ which describes the powder. In the present case, ω and ϕ will be considered to be uniformly distributed between 0 and 2π, and χ distributed according to a probability density $P(\chi)$ such that $\int_0^{\pi/2}P(\chi)d\chi=1$.

For a completely random powder (the case treated by Warren in Ref. 30),

$$P(\chi)=\sin\chi\ .\tag{A3}$$

For ZYX graphite, manufactured by exfoliating a sample of highly oriented pyrolitic graphite, the crystallites have a strong preferential ordering, and $P(\chi)$ is measured by the intensity of the graphite (002) peak in a rocking curve. Such a measurement typically gives a Gaussian profile $I(\Phi)=I_0e^{-(\Phi/\xi)^2}$, with HWHM$=\sqrt{\ln 2}\xi$, on the order of 9°. If this intensity is proportional to the probability that a crystallite has $\chi=\Phi$ with the body $\hat{x}'$ in the scattering plane, then the probability that a crystallite has $\chi=\Phi$ with arbitrary $\hat{x}'\propto e^{-(\Phi/\xi)^2}\sin\Phi$. For ξ somewhat smaller than $\pi/2$, this may be normalized to give

$$P(\chi)=(2/\xi^2)\exp-(\chi/\xi)^2\sin\chi\ .\tag{A4}$$

For Grafoil substrates a combination of (A3) and (A4) has been used.

The powder-averaged intensity $I_P(Q)$ is obtained by substituting (A1) into (A2) and integrating over ω, χ, and ϕ. Hence,

$$I_P(Q)=\int_0^{2\pi}d\omega\int_0^{\pi/2}d\chi\int_0^{2\pi}d\phi P(\chi)I(Q^2\cos^2\psi+q_0^2-2Qq_0\cos\psi\cos\phi)F(Q\sin\psi)\ ,\tag{A5}$$

where the effective tipping angle ψ is defined by $\sin\psi=\sin\omega\sin\chi$, and the coefficient of the $2Qq_0$ term is simplified to the form shown by an appropriate choice for the range of the ϕ integral. For some simple line-shape models, the integral over ϕ can be performed analytically; for now, we define

$$I_c(Q_0)=\int_0^{2\pi}d\phi\, I(Q_0^2+q_0^2-2Qq_0\cos\phi)\ .\tag{A6}$$

We next consolidate the ω and χ integrals by placing the definition of ψ into a Dirac δ function and integrating. This results in

$$I_P(Q)=\int_0^{\pi/2}d\psi\,P'(\psi)I_c(Q\cos\psi)F(Q\sin\psi)\ ,\tag{A7}$$

where

$$P'(\psi)=\cos\psi\int_\psi^{\pi/2}d\chi\,P(\chi)(\sin^2\chi-\sin^2\psi)^{-1/2}\ ,$$

thereby reducing the number of integrals over crystallite orientations from three to two. Because we are presently concerned only with monolayer films, we drop the $F(Q\sin\psi)$ term from the analysis. By taking $P(\chi)$ from (A4) for ZYX, the distribution over effective tipping angle $P'(\psi)$ was integrated numerically and found to be of the form

$$P'(\psi)=(\sqrt{\pi}/\xi)\exp-(\psi/\xi)^2(\cos\psi)^{1/2}\ ,\tag{A8}$$

with a fractional error less than 10^{-3}. For the Warren case of a uniform powder,

$$P'(\psi)=(\pi/2)\cos\psi\ .\tag{A9}$$

For the C peaks, we have used the finite-size model described in the main text. Equation (5) for $I_c(Q_0)$ was substituted into (A7) along with (A8) for the effective vertical mosaic distribution and the integral over ψ performed numerically.

It is of interest to compute several other cases. For a Gaussian peak normalized to unit integrated intensity, the response of one crystallite is

$$I(\vec{Q}')=(\pi\gamma^2)^{-1}\exp[-(|\vec{Q}'-\vec{q}_0|/\gamma)^2]\ ,\tag{A10}$$

and I_c is approximately given by

$$I_c(Q_0)=\gamma^{-1}(\pi Q_0q_0)^{-1/2}\exp\{-[(Q_0-q_0)/\gamma]^2\}\ ,\tag{A11}$$

where the first term in the asymptotic expansion of a Bessel function was used. This is accurate for

$2\gamma^2 Q_0 q_0 \ll 1$. First consider the random powder case. Substituting (A9) and (A11) into (A7), we obtain

$$I_P(Q)=\frac{1}{2\gamma}\left[\frac{\pi}{Qq_0}\right]^{1/2} \times\int_0^{\pi/2} d\psi(\cos\psi)^{1/2}\exp\left[-\left[\frac{Q\cos\psi-q_0}{\gamma}\right]^2\right]. \tag{A12}$$

Following Warren,[27] we note that because the exponential is sharply peaked, $(\cos\psi)^{1/2}$ may be approximated by $(q_0/Q)^{1/2}$. By expanding $\cos\psi$ in the exponential, the intensity reduces to

$$I_P(Q)=(\pi/2\gamma)^{1/2}Q^{-3/2}F[(Q-q_0)/\gamma]\,, \tag{A13}$$

where

$$F(a)=\int_0^\infty \exp[-(x^2-a)^2]dx\,,$$

$$I_P(Q)=\left[\frac{2}{\gamma q_0}\right]^{1/2}\frac{1}{\xi Q}F\left[\frac{Q-q_0}{\gamma}\right]\begin{cases}\exp-(\cos^{-1}q_0/Q)^2/\xi^2, & q_0<Q\\ 1, & q_0\geq Q\,.\end{cases} \tag{A15}$$

This is the modified Warren line shape used in Refs. 31,35, and other work.

This scattering cross section must be convoluted with a spectrometer-resolution function to obtain the experimentally measured intensity,

$$I_{\text{meas}}(\vec{Q})=\int d^3\vec{Q}\,' I_p(\vec{Q}\,')R(\vec{Q}-\vec{Q}\,')\,. \tag{A16}$$

The resolution function is typically a Gaussian ellipsoid,

$$R(\delta\vec{Q})=(\pi^{3/2}\delta K_x\delta K_y\delta K_z)^{-1}\exp[-(\delta Q_x/\delta K_x)^2] \times\exp[-(\delta Q_y/\delta K_y)^2]\exp[-(\delta Q_z/\delta K_z)^2]\,,$$

where δQ_x, δQ_y, and δQ_z are components of $\vec{Q}-\vec{Q}\,'$ along $\vec{Q}$, perpendicular to $\vec{Q}$ in the scattering plane, and perpendicular to the scattering plane, respectively.[53] The δK are controlled by the collimation of the radiation and by the monochromator and analyzer crystals. In general, this convolution has two effects: it broadens the line shape if δK_z is larger than the intrinsic width of the diffraction peak, and it affects the peak intensity through the familiar Lorentz factor. In the present case, $I_p(\vec{Q}\,')$ depends only on the magnitude of $\vec{Q}\,'$ (as long as $\delta Q_z \ll Q$). The transverse resolution integrals therefore drop out. If we let $\delta=\delta K_x$, the longitudinal resolution HWHM/$(\ln 2)^{1/2}$, we can carry out this convolution analytically by noting that

$$\frac{1}{\delta\sqrt{\pi}}\int_{-\infty}^{\infty} dQ'\exp\left[-\left[\frac{Q-Q'}{\delta}\right]^2\right]F\left[\frac{Q'-q_0}{\gamma}\right] =\left[\frac{\gamma^2}{\gamma^2+\delta^2}\right]^{1/4}F\left[\frac{Q-q_0}{(\gamma^2+\delta^2)^{1/2}}\right]. \tag{A17}$$

Therefore, to the level of approximation used in deriving (A13) and (A15), the spectrometer resolution may be incorporated simply by replacing γ by $(\gamma^2+\delta^2)^{1/2}$ in (A13) and (A15).

In the case of *ZYX* substrate, if the effective resolution is on the order of 0.01 Å^{-1} HWHM, as is the case for most of the rotating-anode experiments, the error in regarding $\exp[-(\psi/\xi)^2]$ as a constant over the ψ integral is significant. The resolution can still be integrated analytically. The result is

$$I_S(Q)=\xi^{-1}(\gamma^2+\delta^2)^{-1/2}(Qq_0)^{-1/2} \times\int_0^{\pi/2} d\psi\exp\left[-\left[\frac{\psi^2}{\xi^2}+\frac{[Q-(q_0/\cos\psi)]^2}{\delta^2+(\gamma/\cos\psi)^2}\right]\right]. \tag{A18}$$

This is the form that we have used to fit data from a rotating-anode source with resolution on the order of 0.01 Å^{-1} HWHM.[16]

We wish to check the limiting behavior of (A18) in two important cases. For laboratory x-ray or neutron spectrometers, the longitudinal resolution δ which is determined by slits and/or mosaic crystals, is proportional to $\cos\theta$, where 2θ is the scattering angle. If $\gamma \ll \delta$, this introduces an overall $1/\cos\theta$ term in (A18). If ξ is very small, the peak intensity is then proportional to $(\sin 2\theta)^{-1}$, as expected for a cylinder of scattering. For large ξ, the $\exp[-(\psi/\xi)^2]$ term becomes sensibly constant over the range of integration, and we recover the Warren result that the peak intensity is proportional to $(\sin 2\theta)^{-1}(\sin\theta)^{-1/2}$.

As discussed in the text, we have fitted the *IC*-phase scans with several different line shapes. For a Lorentzian, with $I(Q')=(\kappa^2+|\vec{Q}\,'-\vec{q}_0|^2)^{-1}$,

$$I_c(Q_0)=2\pi[(\kappa^2+Q_0^2+q_0^2)^2-(2Q_0q_0)^2]^{-1/2}\,. \tag{A19}$$

in agreement with Warren's Eq. (36).[52] We have numerically tested the approximations leading to (A13). For a crystallite size of 2000 Å, the results of (A12) and (A13) differ by no more than 5×10^{-4} of the peak intensity. For smaller crystallite sizes, the agreement is slightly worse, 1% at 120 Å (appropriate to Grafoil).

For a Gaussian peak and the vertical mosaic distribution (A8) of *ZYX*, we obtain

$$I_P(Q)=(\xi\gamma)^{-1}(Qq_0)^{-1/2} \times\int_0^{\pi/2} d\psi\, e^{-(\psi/\xi)^2}\exp\left[-\left[\frac{Q\cos\psi-q_0}{\gamma}\right]^2\right]. \tag{A14}$$

We again make the approximation of expanding $\cos\psi$ in the second exponential and replacing ψ in the first exponential by its most probable value, $\cos^{-1}(q_0/Q)$. This results in the expression

In order to perform fits with this form of I_0, we have performed the integral (A7) over ψ numerically. If finite spectrometer resolution must also be taken into account for a Lorentzian line shape, the integrals over Q' and ψ may be performed together as follows. For an arbitrary form of $I_c(Q_0)$, we may write

$$I_S(Q)=\frac{1}{\sqrt{\pi}\delta}\int_{-\infty}^{\infty}dQ'\exp\left[-\left[\frac{Q-Q'}{\delta}\right]^2\right]\int_0^{\pi/2}d\psi\, I_c(Q'\cos\psi)P'(\psi)$$
$$=\frac{1}{\sqrt{\pi}\delta}\int_{-\infty}^{\infty}dQ'\int_0^{\pi/2}d\psi\exp\left[-\left[\frac{Q-(Q'/\cos\psi)}{\delta}\right]^2\right](\cos\psi)^{-1}I_c(Q')P'(\psi)\ .$$

As before, we make use of the fact that the exponential is sharply peaked to replace $\cos\psi$ elsewhere by Q'/Q, and find that for the ZYX substrate,

$$I_s(Q)=Q\int_{-\infty}^{\infty}dQ'I_c(Q')I_P(Q,Q')\ , \tag{A20}$$

where $I_P(Q,Q')$ is given by Eq. (A18), with Q' substituted for q_0 and γ set equal to zero. A similar expression may be derived for an isotropic powder. This is a convenient form for numerical computation, because the parameters entering into $I_P(Q,Q')$, vertical mosaic ξ and spectrometer resolution δ, are generally not free parameters. Hence $I_P(Q,Q')$ may be tabulated and the convolution performed relatively rapidly. The form of (A20) is interesting in that it leads us to regard the substrate vertical mosaic as an element of the spectrometer-resolution function rather than an intrinsic feature of the experimental cross section.

For fluids with very large correlation lengths, the $\sim$2000-Å mean crystallite size will cut off the long tail of the spatial correlation function, leading to a broadening of the scattering peak. One can model this effect by multiplying the assumed spatial correlation function, $r^{-1/2}\exp(-\kappa r)$, by a Gaussian, $\exp[-(r/L)^2]$. This multiplication in real space is equivalent to a convolution in reciprocal space. For the assumed Gaussian form of the finite-size cutoff, this convolution can be incorporated into the spectrometer resolution as discussed above merely by replacing γ or δ by $(\delta^2+\gamma^2)^{1/2}$ in Eqs. (A14) or (A20), as required.

The circular integration can also be performed analytically for the Lorentzian with arbitrary C_4 term and for the square of a Lorentzian. Consider the former. If the intensity from a single crystallite is

$$(\kappa^2+|\vec{Q}'-\vec{q}_0|^2+C_4|\vec{Q}-\vec{q}_0|^4/\kappa^2)^{-1}\ ,$$

and ϕ is defined as the angle between $\vec{Q}'$ and $\vec{q}_0$, then the integral from 0 to $\pi/6$ in ϕ is

$$I_C(Q)=(q_0Q)^{-1}(1-3C_4)^{-1/2}[J(\beta_-)-J(\beta_+)]\ ,$$

where

$$J(\beta)=\frac{2}{\beta}(1+2/\beta)^{-1/2}\tan^{-1}(1+2/\beta)^{-1/2}(2-\sqrt{3})$$

and

$$\beta_\pm=\frac{(q_0-Q)^2}{2q_0Q}+\frac{\kappa^2}{4q_0QC_4}[1\pm(1-3C_4)^{1/2}]\ .$$

The vertical mosaic and (if necessary) spectrometer-resolution integrals were performed numerically as described above.

The Lorentzian-squared line shape is a special case with $C_4=\frac{1}{4}$,

$$\kappa'^2(\kappa'^2+q^2)^{-2}=\tfrac{1}{2}(\kappa^2+q^2+q^4/4\kappa^2)^{-1}\ ,$$

if $\kappa=\kappa'/\sqrt{2}$.

*Present address: Department of Physics and Laboratory for Research on the Structure of Matter, University of Pennsylvania, Philadelphia, PA 19104.

†Present address: Department of Physics, Brookhaven National Laboratory, Upton, NY 11973.

[1]F. C. Frank and J. H. van der Merwe, Proc. R. Soc. London, Ser. A 198, 205 (1949); 198, 216 (1949).

[2]P. Bak, D. Mukamel, J. Villain, and K. Wentowska, Phys. Rev. B 19, 1610 (1979).

[3]V. L. Pokrovsky and A. L. Talapov, Phys. Rev. Lett. 42, 65 (1979); Zh. Eksp. Teor. Fiz. 78, 269 (1980) [Sov. Phys.—JETP 51, 134 (1980)]; a more transparent discussion is given by M. E. Fisher and D. S. Fisher, Phys. Rev. B 25, 3192 (1982).

[4]A. R. Kortan, A. Erbil, R. J. Birgeneau, and M. S. Dresselhaus, Phys. Rev. Lett. 49, 1427 (1982).

[5]J. Villain, in *Ordering in Strongly Fluctuating Condensed Matter Systems*, edited by T. Riste (Plenum, New York, 1980), p. 221.

[6]S. N. Coppersmith, D. S. Fisher, B. I. Halperin, P. A. Lee, and W. F. Brinkman, Phys. Rev. Lett. 46, 549 (1981); 46, 869 (E) (1981); Phys. Rev. B 25, 349 (1982); see also S. Ostlund, *ibid.* 24, 398 (1981).

[7]F. F. Abraham, S. W. Koch, and W. E. Rudge, Phys. Rev. Lett. 49, 1830 (1982); F. F. Abraham, W. E. Rudge, D. J. Auerbach, and S. W. Koch, *ibid.* 52, 445 (1984).

[8]J. Villain and P. Bak, J. Phys. (Paris) 42, 657 (1981).

[9]M. Kardar and A. N. Berker, Phys. Rev. Lett. 48, 1552 (1982).

[10]D. A. Huse and M. E. Fisher, Phys. Rev. Lett. 49, 793 (1982); Phys. Rev. B 29, 239 (1984).

[11]P. Bak, Phys. Rev. Lett. 46, 791 (1981).

[12]V. L. Pokrovsky, J. Phys. (Paris) 42, 761 (1981).

[13]P. Bak, Rep. Prog. Phys. 45, 587 (1982).

[14]A. Thomy, J. Regnier, and X. Duval, in Colloq. Int. Cent. Nat. Rech. Sci 201, 511 (1972); A. Thomy, J. Regnier, J. Menaucourt, and X. Duval, J. Cryst. Growth 13, 159 (1972); A. Thomy and X. Duval, J. Chim. Phys. 67, 1101 (1970).

[15]M. D. Chinn and S. C. Fain, Jr., Phys. Rev. Lett. 39, 146 (1977).

[16]P. W. Stephens, P. Heiney, R. J. Birgeneau, and P. M. Horn,

Phys. Rev. Lett. 43, 47 (1979).
[17]J. B. Hastings and D. E. Moncton, Bull. Am. Phys. Soc. 24, 407 (1979).
[18]S. C. Fain, Jr., M. D. Chinn, and R. D. Diehl, Phys. Rev. B 21, 4170 (1980).
[19]P. S. Schabes-Retchkiman and J. A. Venables, Surf. Sci. 105, 536 (1981), and references therein.
[20]H. Shiba, J. Phys. Soc. Jpn. 46, 1852 (1979); 48, 211 (1980); the rotation of incommensurate phases was first predicted by A. D. Novaco and J. P. McTague, Phys. Rev. Lett. 38, 1286 (1977).
[21]J. Villain, Surf. Sci. 97, 219 (1980); J. Villain, J. Phys. (Paris) Lett. 41, L267 (1980); V. L. Pokrovsky and A. L. Talapov, Solid State Commun. 33, 749 (1980).
[22]M. Nielsen, J. Als-Nielsen, J. Bohr, and J. P. McTague, Phys. Rev. Lett. 47, 582 (1981).
[23]D. E. Moncton, P. W. Stephens, R. J. Birgeneau, P. M. Horn, and G. S. Brown, Phys. Rev. Lett. 46, 1533 (1981).
[24]D. M. Butler, J. A. Litzinger, and G. A. Stewart, Phys. Rev. Lett. 44, 466 (1980).
[25]*ZYX* is manufactured by Union Carbide Corporation, Carbon Products Division, Parma, Ohio.
[26]R. J. Birgeneau, G. S. Brown, P. M. Horn, D. E. Moncton, and P. W. Stephens, J. Phys. C 14, L49 (1981).
[27]R. J. Birgeneau, P. A. Heiney, and J. P. Pelz, Physica 109&110B, 1785 (1982).
[28]P. A. Heiney, R. J. Birgeneau, G. S. Brown, P. M. Horn, D. E. Moncton, and P. W. Stephens, Phys. Rev. Lett. 48, 104 (1982); Phys. Rev. B 28, 6416 (1983).
[29]D. E. Moncton and G. S. Brown, Nucl. Instrum. Methods 208, 579 (1983).
[30]B. E. Warren, Phys. Rev. 59, 693 (1941).
[31]J. K. Kjems, L. Passell, H. Taub, J. G. Dash, and A. D. Novaco, Phys. Rev. B 13, 1446 (1976).
[32]Reference 26 mistakenly asserted that a solid with a sharp cutoff would have q^{-2} tails in all directions.
[33]We have estimated the curvature of the Kr-graphite potential from the central and saddle-point potential energies of W. Steele [Surf. Sci. 36, 317 (1973)]; the resulting spring constant ξ is 8 dyn/cm.
[34]G. Theodorou and T. M. Rice, Phys. Rev. B 18, 2840 (1978).
[35]P. M. Horn, R. J. Birgeneau, P. Heiney, and E. M. Hammonds, Phys. Rev. Lett. 41, 961 (1978).
[36]J. G. Dash and R. D. Puff, Phys. Rev. B 24, 295 (1981).
[37]B. Jancovici, Phys. Rev. Lett. 19, 20 (1967); Y. Imry and L. Gunther, Phys. Rev. B 3, 3939 (1971).
[38]D. E. Moncton and R. Pindak, Phys. Rev. Lett. 43, 701 (1979).
[39]P. Dutta and S. K. Sinha, Phys. Rev. Lett. 47, 50 (1981).
[40]D. S. Fisher (private communication).
[41]E. Specht (private communication).
[42]H. Yoshizawa, R. A. Cowley, G. Shirane, R. J. Birgeneau, H. Guggenheim, and H. Ikeda, Phys. Rev. Lett. 48, 438 (1982).
[43]J. Als-Nielsen, R. J. Birgeneau, M. Kaplan, J. D. Litster, and C. R. Safinya, Phys. Rev. Lett. 39, 352 (1977).
[44]M. Nielsen, J. Als-Nielsen, and J. P. McTague, in *Ordering in Two Dimensions,* edited by S. K. Sinha (Elsevier, New York, 1981), p. 135.
[45]A. W. Overhauser, Phys. Rev. B 3, 3173 (1971).
[46]C. Marti and T. Ceva, Phys. Rev. Lett. 49, 1678 (1982).
[47]Y. Larher, J. Chem. Phys. 68, 2257 (1978).
[48]F. A. Putnam and T. Fort, Jr., J. Phys. Chem. 79, 459 (1975).
[49]This number is in satisfactory agreement with the isosteric heat of adsorption in the *C* phase deduced from the vapor-pressure isotherms of Ref. 14.
[50]This is the crystallographic convention. Our ω, χ, and ϕ are defined as ϕ, θ, and ψ, respectively, by Goldstein.[51] We reserve 2θ for the scattering angle and ψ for the effective tipping angle, in accordance with previous work.
[51]H. Goldstein, *Classical Mechanics,* 2nd ed. (Addison-Wesley, Reading, Mass., 1980).
[52]We have not carried through the form factor, unit-cell volume, Debye-Waller factor, or other terms required to obtain the total scattered intensity. Warren's analysis contains a polarization term $1 + \cos^2(2\theta)$ for an unpolarized beam; this term is absent in a synchrotron x-ray source with vertical scattering vector.
[53]This coordinate system is not to be confused with that discussed at the beginning of the Appendix, as the crystallite *c* axis is not necessarily perpendicular to the scattering plane.